DEFENCE DÉFENSE

Development of a Portable High-Frequency Radar

Harold Wilson
Defence Research Establishment Ottawa

DEFENCE RESEARCH ESTABLISHMENT OTTAWA

TECHNICAL REPORT
DREO TR 1999-108
October 1999

National Defence Défense nationale

Canada

DEFENCE DÉFENSE

Development of a Portable High-Frequency Radar

Harold Wilson
Ground Based Radar Group
Surface Radar Section

DEFENCE RESEARCH ESTABLISHMENT OTTAWA

TECHNICAL REPORT
DREO TR 1999-108
October 1999

Project
05AB11

Abstract

The Surface Radar Section of DREO is developing a portable HF radar. The report presents an overview of the radar and analysis of a series of tests done in 1998. The equipment including antennas and electronics is described. A series of electronics problems was encountered, but none of them have a significant effect on the operation of the system. The receiver system was calibrated using loopback runs, source measurements and meteor reflections. Measurements of interference, meteors and environmental clutter at 24.5 MHz are presented. The results of the tests are used to estimate the performance of the portable radar in Line-of-Sight mode against theatre ballistic missiles.

Résumé

La Section du radar de surface du CRDO travaille au développement d'un radar HF portable. Ce rapport présente un aperçu de ce radar ainsi qu'une analyse d'une série d'essais effectués en 1998. Le matériel présenté comprend les antennes et les dispositifs électroniques. Ces derniers ont posé une série de problèmes qui n'ont toutefois pas nui de manière significative au fonctionnement du système. Le récepteur a été étalonné en utilisant des configurations en boucle, des mesures à la source et des réflexions de météores. Le rapport présente des mesures de brouillage, de météores et de fouillis environnemental à 24,5 MHz. Les résultats de ces essais sont utilisés afin d'estimer les performances du radar portable en visibilité directe contre les missiles balistiques de théâtre.

Executive Summary

Background

The Surface Radar Section of Defence Research Establishment Ottawa has been investigating applications of High-Frequency Radar for the past ten years. To date, DREO's efforts have been directed mainly toward the development of 3-6-MHz surface-wave radars for maritime surveillance, under a Major Development Project with Raytheon Canada, and this project has led to the installation of demonstration models in Newfoundland. As part of the maritime surface-wave-radar program, Raytheon Canada developed a set of HF-radar electronics and software for controlling the electronics.

With the surface-wave-radar program nearing completion, the Surface Radar Section is now considering other applications of HF radar. The first step in this program has been the construction of a portable HF radar which can be applied to detection of ascending theatre ballistic missiles and as a portable coastal surveillance radar. In 1997, Raytheon Canada installed in a trailer a set of HF-radar electronics owned by DREO, and these electronics were used by the University of Western Ontario in a meteor-observation experiment. In 1998 a set of vertically-polarized antennas was built and the complete portable system was installed at Shirley's Bay, Ottawa, and tested by DREO.

This report describes the development of the portable HF radar to date and summarizes the results of the tests and measurements made in 1998.

Principal Results

The 24.5-MHz antennas that were built for the tests performed in accordance with numerical predictions.

The tests demonstrated a method for calibrating the receive array using meteor trails as distant point sources. The receiver and environmental noise was measured. Long-range reflections due to mesospheric and stratospheric turbulence, or perhaps to the ionosphere, were observed in tests at 24.5 MHz.

The system is ready for use detecting ascending TBM's at ranges of ~250 km.

Significance of Results

The electronics and 24.5-MHz antennas are ready for tests with TBM targets and sounding rockets. With a new set of antennas operating in the 8-15 MHz range, it will be ready for a demonstration as a portable coastal surveillance radar

Wilson, Harold S., "Development Of A Portable High-Frequency Radar", DREO TR 1999-108, Defence Research Establishment Ottawa

Sommaire

Historique

La Section du radar de surface du Centre de recherches pour la Défense Ottawa a étudié les applications du radar hautes fréquences de surface pendant les dix dernières années. Jusqu'à présent, les efforts du CRDO ont porté principalement sur le développement de radars à onde de surface entre 3 et 6 MHz pour la surveillance maritime dans le cadre d'un projet majeur de développement entrepris avec Raytheon Canada. Ce projet a mené à l'installation de modèles de démonstration à Terre-Neuve. Dans le cadre du Programme de radar à onde de surface maritime, Raytheon Canada a développé un ensemble électronique de radar HF ainsi que le logiciel de commande de cet ensemble.

Étant donné que le programme du radar à onde de surface approchant de sa fin, la Section du radar de surface envisage d'autres applications du radar HF. La première étape de ce programme a consisté à fabriquer un radar HF portable qui peut être utilisé pour la détection de missiles balistiques de théâtre en ascension et comme radar de surveillance côtière portable. En 1997, Raytheon Canada a installé dans une roulotte un ensemble électronique de radar HF appartenant au CRDO et ces appareils électroniques ont été utilisés par la University of Western Ontario dans une expérience d'observation de météores. En 1998, un ensemble d'antennes à polarisation verticale a été fabriqué. L'ensemble portable complet a été installé à Shirley's Bay, à Ottawa, et le CRDO en a fait l'essai.

Le présent rapport décrit le processus de développement du radar HF jusqu'à présent et il résume les résultats des essais et mesures réalisés en 1998.

Principaux résultats

Les antennes à 24,5 MHz fabriquées pour les essais ont fonctionné conformément aux prévisions numériques.

Les essais ont permis de faire la démonstration d'une méthode d'étalonnage du réseau de réception faisant appel aux trainées météorique comme sources ponctuelles distantes. Le bruit du récepteur et les bruits environnementaux ont été mesurés. Des réflections dues aux turbulences mésosphériques et stratosphériques, ou peut être à l'ionosphére, ont été observées lors d'essais à 24,5 MHz.

Le système est prêt à être utilisé pour la détection de missiles balistiques de théâtre (MBT) en ascension à des distances d'environ 250 km.

Signification des résultats

Les dispositifs électroniques et les antennes à 24,5 MHz sont prêts pour réaliser des essais avec des MBT ou des fusées de sondage. Avec un nouvel ensemble d'antennes pour la plage 8-15 MHz, ils pourront servir à des démonstrations comme radar de surveillance côtière portable.

Wilson, Harold S., "Development Of A Portable High-Frequency Radar", DREO TR 1999-108,
Defence Research Establishment Ottawa

Table of Contents

List of Figures

List of Figures (cont.)

List of Tables

1. Introduction

The Surface Radar Section of Defence Research Establishment Ottawa has been investigating applications of High-Frequency Radar for the past ten years. To date, DREO's efforts have been directed mainly toward the development of 3-6-MHz surface-wave radars for maritime surveillance, under a Major Development Project with Raytheon Canada, and this project has led to the installation of demonstration models in Newfoundland. As part of the maritime surface-wave-radar program, Raytheon Canada developed a set of HF-radar electronics and software for controlling the electronics.

With the surface-wave-radar program nearing completion, the Surface Radar Section is now considering other applications of HF radar. The first step in this program has been the construction of a portable HF radar which can be applied to detection of ascending theatre ballistic missiles and as a portable coastal surveillance radar. In 1997, Raytheon Canada installed in a trailer a set of HF-radar electronics owned by DREO, and these electronics were used by the University of Western Ontario in a meteor-observation experiment. In 1998 a set of vertically-polarized 24.5-MHz antennas was built and the complete portable system was installed and tested at Shirley's Bay, Ottawa in the late summer and autumn of 1998.

This report describes the development of the portable HF radar to date and summarizes the results of the tests and measurements made in 1998.

Section 2 describes the simple transmit and receive antennas which were designed for operation in the 24-25 MHz region. Section 3 provides a general description of the radar electronics, and Section 4 makes some observations on the design of the digital filters that are incorporated in Raytheon Canada's digital receivers. Section 5 discusses system noise and calibration. The measurements of external noise and interference, meteor reflections, and environmental clutter are discussed in Section 6. This completes the description of the system and tests.

Section 7 estimates the performance of the system in detecting small ballistic missiles (Theatre Ballistic Missiles (TBMs)) and discusses briefly possible improvements to the system to optimize TBM detection. Section 8 summarizes the report and concludes that the system is ready for tests with sounding-rocket targets.

2. Antennas

It was envisaged that the first application of the portable HF radar would be in detecting a launch of a Black Brant sounding rocket. It was decided that the measurements would be performed at a single frequency near 24.5 MHz, and consequently simple 2-element vertical dipole Yagi-Uda antennas were designed since a broad frequency range was not required. This section describes the electrical and mechanical design of the antennas, compares calculated and measured antenna behaviour, and estimates the behaviour of the 8-element receive array.

2.1 Antenna design

The antennas were designed and built by Petrie Telecommunications Ltd. The choice of simple 2-element vertical-dipole Yagi antennas was based on the following considerations :

1. A 50-Ω antenna impedance was desired in order to make it unnecessary to use a matching network to couple the antennas to 50-Ω cables, transmitter outputs and receiver inputs. It is difficult to achieve an antenna impedance near $(50+j0)$ Ω with a simple dipole or with 3 or more elements in the antenna.
2. We wanted low gain in the backward direction in order to reduce sensitivity to targets and sources of interference behind the antennas.
3. The wavelength was ~12 m, so half-wavelength dipole components were feasible. This meant that a ground screen was not required.
4. A vertical antenna was chosen because the first two applications envisaged for the system were detection of ascending small missiles, and short-range coastal surveillance using surface waves. In both cases a vertical electric field is required.

The Numerical Electromagnetics Code (NEC, Ref. [1]) was used to estimate the impedance and radiation pattern of the antennas. NEC is a widely-available computer program which applies integral-equations to determine the currents induced on a conducting structure by various excitations and loads. It is well suited to calculating the behaviour of structures with dimensions up to several wavelengths such as the simple antennas described here. NEC also incorporates two methods for including the effect of ground permittivity and conductivity : (i) Sommerfeld's solution for the electromagnetic field of a source above a conducting half-space is included in the field calculations, (See Ref.[1], Part II for further references) and (ii) a simpler, faster and somewhat less accurate estimate that assumes the field is simply reflected from the ground ("Reflection Coefficient Approximation").

Figure 1 is a sketch of the antenna. It is not, in fact, a simple 2-element Yagi because the vertical support, the antenna grounding wire, the horizontal crossbar and the coaxial-cable shields all radiate. There is no attempt to balance the feedline. Even if the vertical support were non conducting, currents excited on the shield of the coaxial feedline would result in the antenna radiation pattern being different from the what is usually expected of a 2-element Yagi. The dimensions of the antenna elements were determined by adjusting the lengths and positions of the antenna components until NEC indicated that the desired impedance of $(50+j0)$-Ω at 24.5 MHz had been achieved.

The total weight of the antenna is ~46 kg of which ~32 kg is the wood base.

Figure 2 shows the calculated antenna impedance in the range 24-25 MHz, and the usual measures of antenna response (VSWR, reflection losses). For the calculations shown in Figure 2, NEC used the Sommerfeld solution to include the effects of ground conductivity and permittivity which were set to $\sigma=10^{-3}$ S/m and $\varepsilon=10$ respectively. The results changed only slightly when the calculations were performed with the ground taken to be a simple reflector ("Reflection Coefficient Approximation"), and when σ was varied through the range 10^{-4} - 10^{-2} S/m and ε from 10 - 20. The small jumps in the plot of antenna impedance are the result of small errors in NEC's calculations of the integrals in the Sommerfeld theory.

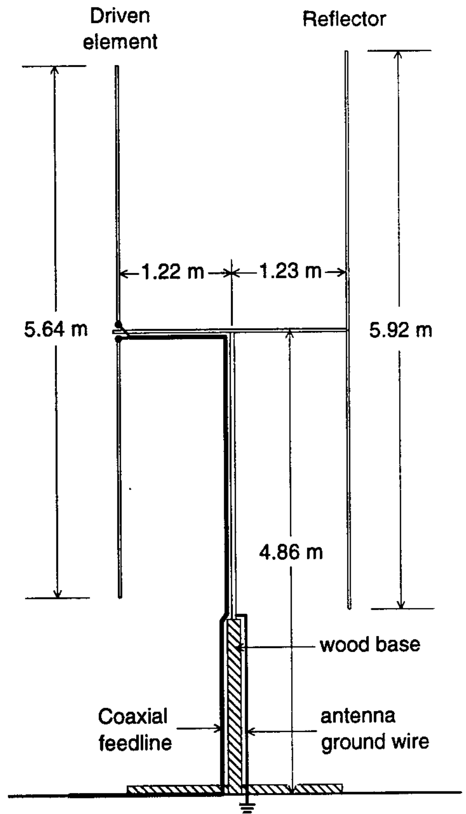

Figure 1. Sketch of the antenna used with the portable HF radar. Except for the wood base, it is fabricated from aluminum tubing. The dimensions were chosen to get 50-Ω impedance at 24.5 MHz.

A major advantage of NEC is that it is easy to calculate accurately the radiation pattern of an antenna and removes the need to measure the pattern, at least for simple structures such as this one. At frequencies in the 20-30 MHz range, measurements of the radiation pattern at significant elevation angles and ranges of more than a few wavelengths is quite difficult : because of the heights and distances involved, a calibrated source must be towed from an airplane. Since NEC is an electrodynamically correct model of thin-wire structures, its results are reliable subject to knowledge of the environment (i.e. the ground permittivity and conductivity), the accuracy of the model, and the degree to which the antenna components satisfy the thin-wire limitations. The effect of small errors can be checked by varying the model parameters, and as a result, we can have confidence that NEC provides accurate estimates of antenna performance, without the trouble and expense of radiation-pattern measurements.

Figure 3 gives the radiation patterns for the antenna at 24.1, 24.5 and 24.9 MHz. The front/back ratio of the antennas is not particularly large : it rises from 5.5 dB at 24.1 MHz to 10 dB at 25.3 MHz. The gain minimum at 110°-130°, which lies at least 13 dB below the maximum at 0°, will be useful for suppressing local interference.

Figure 4 shows the results of two simple measurements of the antenna's impedance mismatch. In the first measurement, a signal generator, a directional combiner and a signal analyzer were used to measure the power of the signal reflected from the antenna. Figure 4(a) shows that the minimum reflection occurred at 24.35 MHz rather than at 24.48 MHz as predicted by NEC, and that the reflected power was ~32 dB below the incident power (i.e. the antenna impedance was within ~2 Ω of

the perfect-match of $(50+j0)\Omega$). This is a small difference that we attribute to imprecision in modeling the coaxial feedline and the antenna ground wire, and details of the antenna setup. Petrie Telecommunications measured the minimum reflection at 24.52 MHz. Figure 4(a) shows that the antenna impedance is very close to 50 Ω with the antenna reflecting $<4\times10^{-3}$ of the incident power between 24.25 and 24.45 MHz. The reflected signal when the antenna was replaced with a 50-Ω terminator is included to show the minimum apparent reflected signal that could be measured with this method.

The portable radar transmitter consists of 4 Analogic 6082C power amplifiers whose outputs are combined and fed to the transmit antenna on a 100-m LDF4 Heliax coaxial cable. The antenna-impedance mismatch was estimated using meters on the amplifiers which are provided to measure reflected power. Figure 4(b) shows the reflected power measured at the amplifier meters as a function

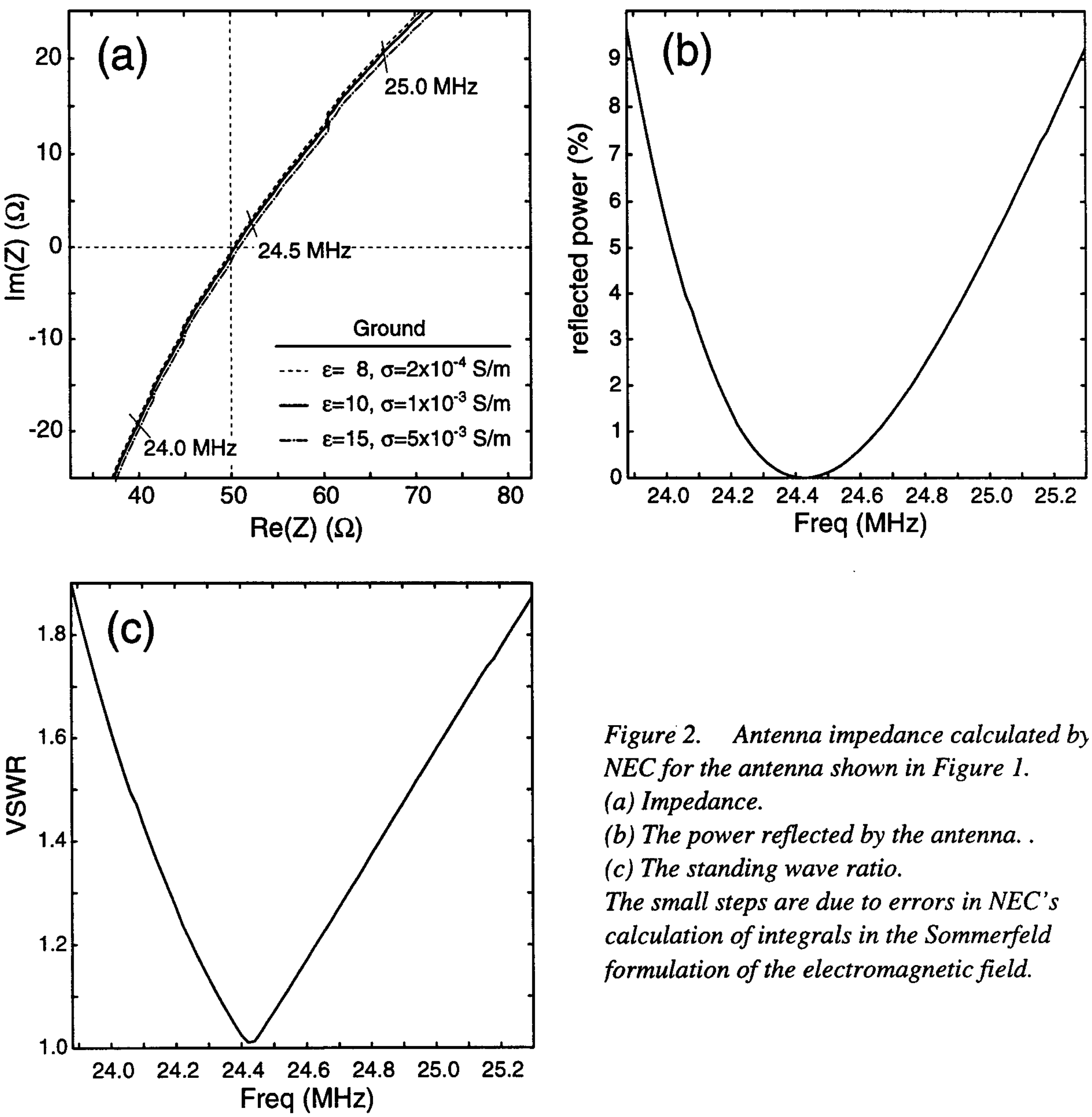

Figure 2. Antenna impedance calculated by NEC for the antenna shown in Figure 1.
(a) Impedance.
(b) The power reflected by the antenna. .
(c) The standing wave ratio.
The small steps are due to errors in NEC's calculation of integrals in the Sommerfeld formulation of the electromagnetic field.

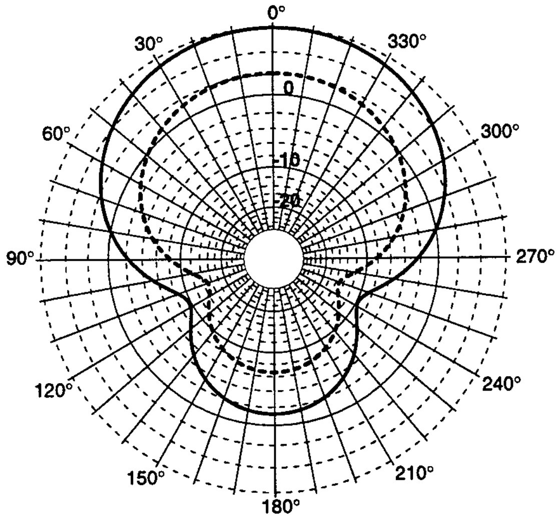

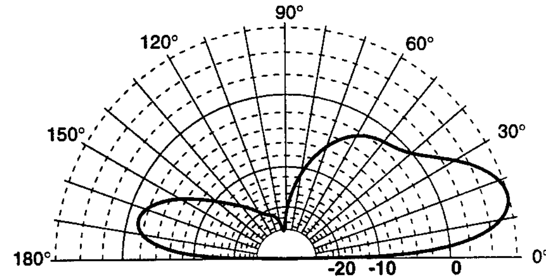

24.1 MHz

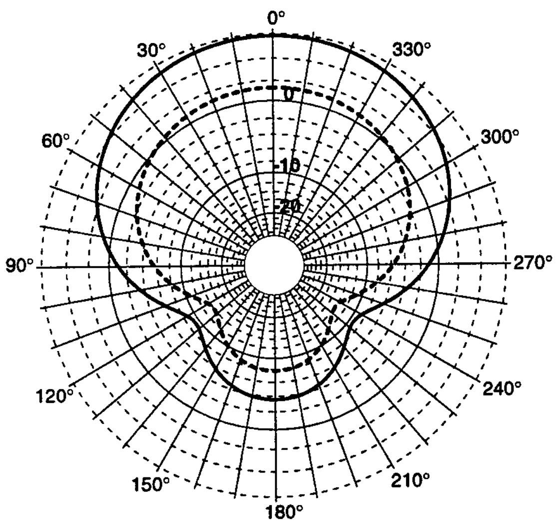

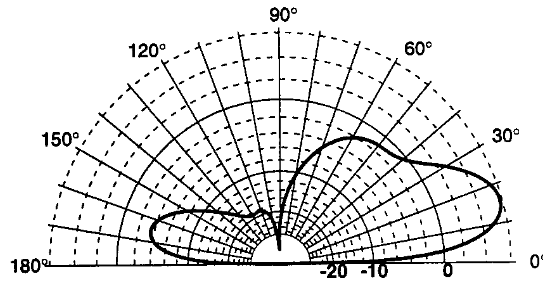

24.5 MHz

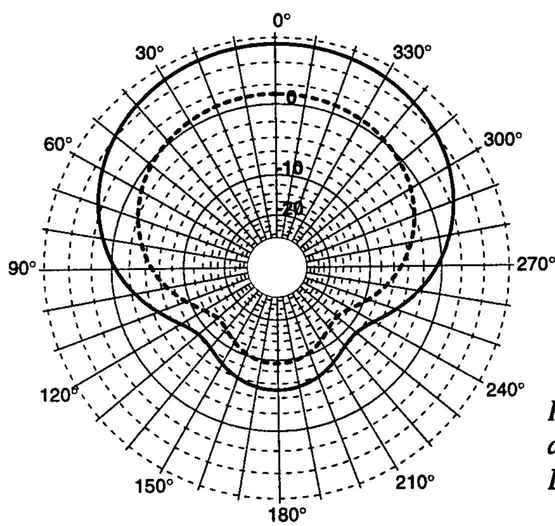

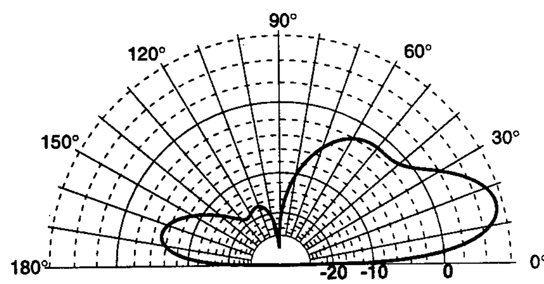

24.9 MHz

Figure 3. Radiation patterns calculated by NEC for the antenna shown in Figure 1 at 24.1, 24.5 and 24.9 MHz.
Left : azimuthal patterns. Solid : $\theta=16°$ elevation
Dashed : $\theta=5°$
Right : elevation pattern. $\phi=0°/180°$.

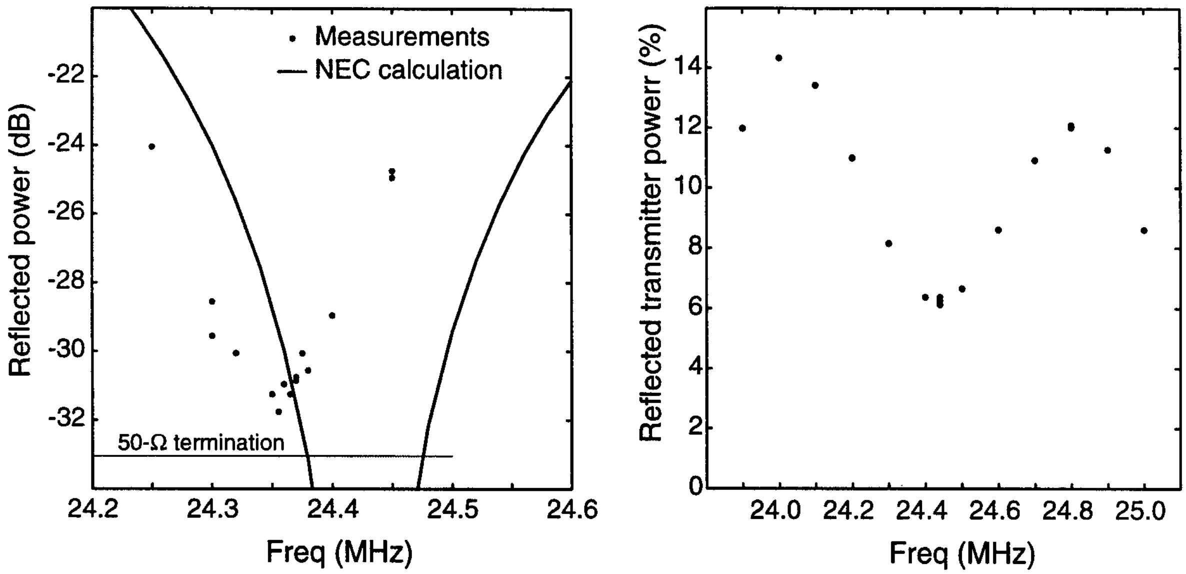

Figure 4. Reflection losses with the antenna shown in Figure 1.

(a) The power reflected from the antenna measured using a directional coupler and a signal analyzer. The line labeled "50-Ω termination" shows the signal-analyzer output when the antenna was replaced by a 50-Ω resistor.

(b) The power reflected back to the transmitters as measured by the meters on the Analogic 6082C power amplifiers.

of frequency. Even with a nearly-perfectly-matched antenna at ~24.5 MHz, the amplifiers indicate ~6% reflected power. We attribute this to mismatches in the combiner which sums the outputs of the 4 amplifiers, or to errors in the circuit that measures the reflected power. It is interesting that the reflected power drops when the frequency falls below 24.0 MHz or exceeds 24.8 MHz. This probably indicates constructive and destructive interference between the waves reflected from the combiner and from the antenna.

2.2 Transmit antenna

The transmit antenna consisted of a single 2-element Yagi antenna as shown in Figure 1 and as described in Section 2.1 above. This allowed the system to illuminate a broad sector in azimuth (±65°) but provided only ~8.5 dB gain reduction in the backward direction. It also meant that there was no need to install power splitters for the transmitter, nor was there any concern about the power and phase balance between the transmitter elements.

In most of the applications envisaged for the HF portable radar, it is anticipated that the system will perform surveillance of a large area, and a broad-azimuth transmit beam will be required. Thus the single-element transmit-antenna configuration is probably close to what will be used in a more advanced system.

2.3 Receive antenna array

The receive array for the test program was a line of 8 of the elements shown in Figure 1 with 6-m spacing (0.49 λ at 24.5 MHz). For multi-component elements like these, the distribution of currents on the antenna elements changes with the direction of the incoming signal. In addition, the current distribution excited on one element of the array by re-radiation from a neighbouring element is different from the current distribution excited by the signal. This makes it difficult to estimate the effect of array couplings, but, in a closely-spaced array like this, inter-element coupling may have a significant effect on the gains and phases of the antenna outputs.

To investigate the effect of coupling on the array response, NEC was used to model the complete 8-element receive array at 24.5 MHz. This was a brute-force solution of the problem, but it did not impose a large computational load on the computer (an Alpha Station 400) and it was an easy way to determine the effect of antenna coupling without making any assumptions about each element's response to currents excited in the other elements. Figure 5 shows the result of NEC modeling for plane waves coming from θ=10° above the horizon and azimuth angles -90°≤ϕ≤90° (i.e. the forward direction of the antenna). The apparent incident angle ("apparent α") is the source direction determined by a linear fit to the phases of the array elements :

$$\text{apparent } \alpha = \arcsin\left(\frac{[\text{phase per element}]}{kd}\right) \quad . \tag{1}$$

where k=2π/λ and d is the spacing between elements of the linear array. The true incident angle is given by geometry :

$$\text{true } \alpha = \arcsin(\cos\theta \sin\phi) \quad . \tag{2}$$

The phase convention is that positive relative phase means that the signal arrives at an earlier time, and positive α corresponds to signals arriving from the element-8 end of the array (left of boresight). The phase error in Figure 5(a) is the difference between an element's phase and the straight-line fit to the relative phases of elements 2 through 7. (Straight-line fits to elements 1 through 8 yielded the same slope but a different phase offset. Consequently, including all 8 array elements would simply bend the plot in Figure 5(a) down at large |α| and up by ~1.2° at α=0, but there would be no change in the phase difference between elements for a particular source direction.) The relative gain in Figure 5(b) is normalized so that

$$\sum_{k=1}^{8} (\text{relative gain}_k)^2 = 8$$

That is, the variation in total sensitivity with α (i.e. the radiation pattern) has been removed, so Fig 5(b) shows the gain of each element relative to the other elements at a given angle. Figures 5(a,b) show that the effects of interelement coupling are not serious except for the end elements (1 and 8), where the relative gain is in error by ~2 dB for |α|>45°, and the phase relative to the other elements is advanced by 10-20°.

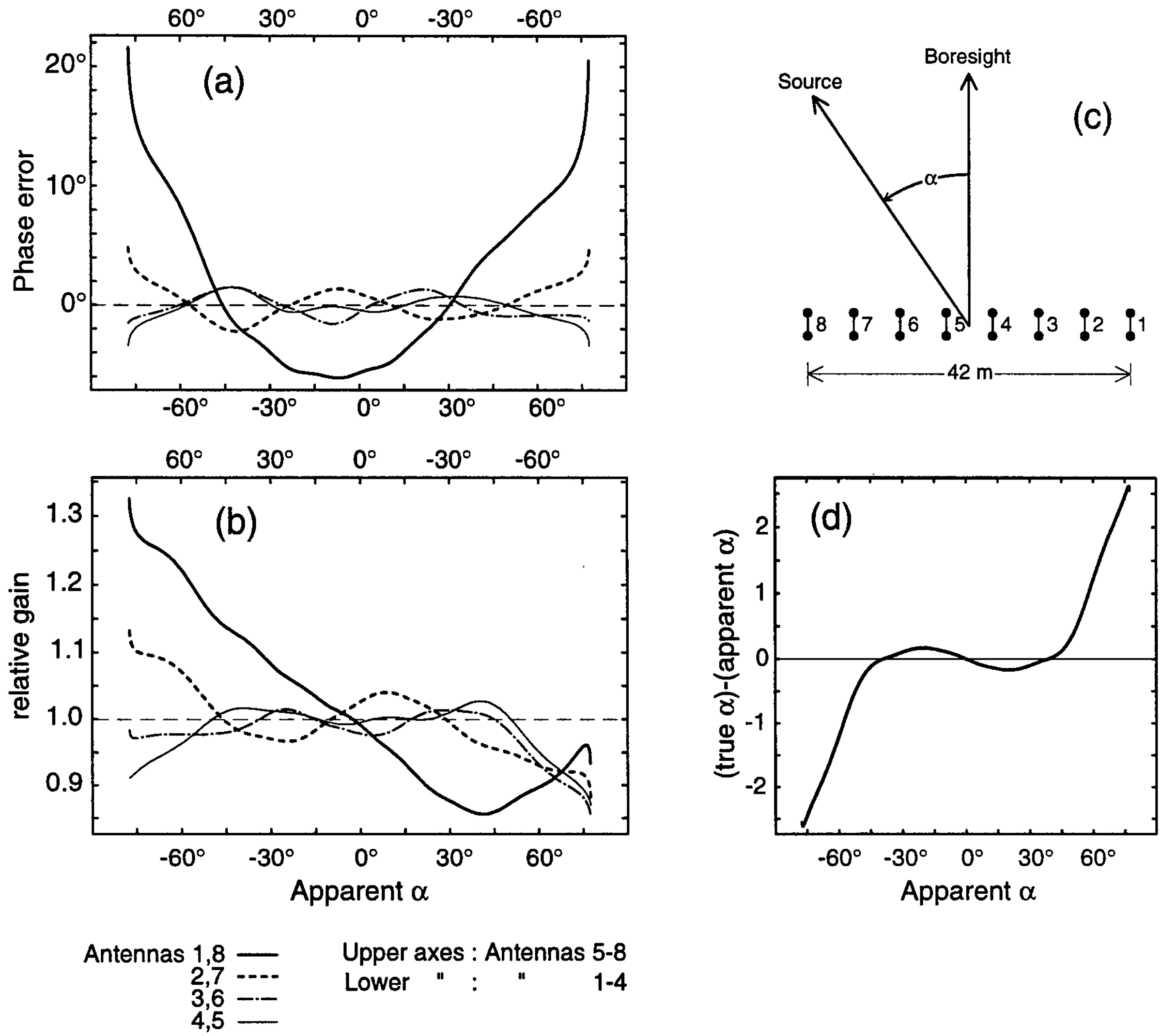

Figure 5. The effect of inter-element coupling on the response of an 8-element linear array. The source direction is θ=10° above the horizon with azimuth range -90°≤ϕ≤90°. "Apparent α" is the angle left of the boresight estimated from a straight-line fit to the phases of elements 2-7.

(a) The phase error is the difference between element phase and a straight-line fit to the phases of elements 2-7.

(b) The relative gain is normalized so Σ(relative gain)^2=8 at each angle.

(c) A sketch showing the array layout. α is the source bearing relative to the boresight plane.

(d) The error in estimates of the source direction.

The phase error in elements 1 and 8 seems to be fairly large, but it must be compared to the phase difference between elements. For d=6 m, f=24.5 MHz and α=60°, the phase difference between adjacent elements is 153°, and a 15° error in elements 1 and 8 will not change the estimate of phase/element (i.e. "apparent α") by very much, and it will not broaden the array beam width significantly. However, Figure 5(d) shows that the array coupling introduces a systematic error in the estimate of source direction reaching almost 2° at a true souce direction of ~67° (apparent bearing α=69° , elevation angle θ=10°).

2.4 Antenna cables

The receive antennas were connected to the radar electronics by 100-m lengths of RG213 cable. The cables were cut to the same phase length to within ~5 cm (~2° in phase) in order to reduce uncertainties in the interpretation of signal phases. The signal loss on the cables at 24.5 MHz was 3.5 dB.

For the transmit antenna, a 100-m LDF4-50 Heliax cable was used, giving a loss of 1.1 dB at 24.5 MHz.

The cable attenuation greatly exceeds the signal loss due to antenna-impedance mismatches.

3. Radar Electronics

3.1 Block Diagram and Overview

The system tested here uses Raytheon Canada's SWR-503 HF radar electronics which were developed for the HF Surface-Wave Radar program and which have been installed in demonstration surveillance radars at Cape Race and Cape Bonavista in Newfoundland. It is a monostatic pulse-Doppler radar.

Figure 6 is a simplified block diagram of the system. The Timing Control Unit uses a 50-MHz oscillator to determine basic time steps and to control the system. The intermediate frequency f_{IF} must be 300 kHz and the ADC sample rate must be exactly $4/3 \times f_{IF}$ in order to separate the in-phase and quadrature components of the signal. The only adjustable frequency in the system is the carrier frequency f_0 which is determined by setting an oscillator to the frequency $f_0+f_{IF}+50$ MHz.

The mixing/amplification stage is a standard double heterodyne system in which the incoming signal at frequency f_0 is mixed with $f_0+f_{IF}+50$ MHz giving $f_{IF}+50$ MHz and then with 50 MHz giving f_{IF}. Following the first mixer, the signal is filtered with a crystal-controlled 50.25-50.35 MHz bandpass filter. Thus the system operates only with f_{IF} =300 kHz and bandwidth ±50 kHz.

On command from the Timing Control Unit, the pulse generator generates a low-voltage ($2V_{pp}$) pulse at the carrier frequency with an envelope specified by the user. The transmitter amplifiers and combiner produce the high-power pulse (up to 1800 V_{pp}) which drives the transmit antenna.

In the system configuration tested in 1998, the pulse shapes were limited to binary-phase coded pulses. In the future it is expected that the software and the pulse-compression hardware will be modified to allow stepped FM and continuous-wave FM pulses.

The outputs of the digital filters were written directly to disk for off-line analysis, and there was no on-line data analysis or display in this experimental system.

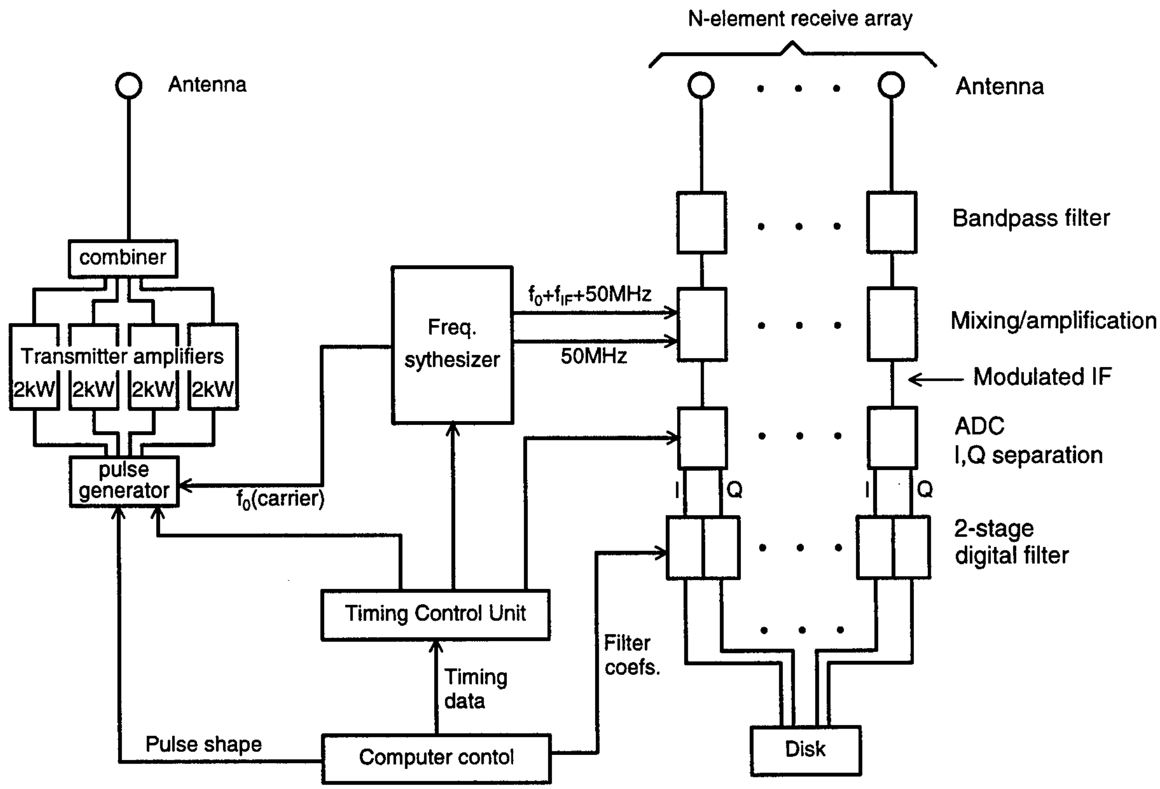

Figure 6. A block diagram of the radar electronics.

3.2 Receiver electronics and data acquisition

The receiver electronics are shown on the right side of Figure 6. The antennas were connected directly by 100-m RG213 coaxial cables to the receiver electronics without matching networks since the antennas were designed to have 50+j0 Ω impedance near 24.5 MHz (see Section 2.1 above). The input bandpass filters (20-35 MHz) were intended principally to remove local AM and FM broadcast signals so that the receivers would not be overloaded in subsequent stages. Section 3.1 discussed the two-stage mixing and amplification that shifted the frequency from the carrier f_0~24.5 MHz to f_{IF}=300 kHz.

The SWR-503 radar uses a single 16-bit ADC sampling the modulated IF at a rate of exactly $4/3\, f_{IF}$. At this sample rate, the ADC output gives directly the real and imaginary (= in-phase I and quadrature Q) components of the received carrier modulation. Suppose that the input to the ADC is

$$S(t) = \mathrm{Re}\Big[\big(I(t) + jQ(t)\big)e^{j2\pi f_{IF}t}\Big] \tag{3a}$$

and the sampling period is τ, so the ADC output is

$$S_k = S(k\tau) \quad . \tag{3b}$$

Analysis of equations(3a,b) shows that, with the sampling period $\tau = 3/4f_{IF}$, the ADC output S_k gives I and Q directly :

$$\ldots \quad S_0 = I_0 \quad S_1 = Q_1 \quad S_2 = -I_2 \quad S_3 = -Q_3 \quad S_4 = I_4 \quad \ldots \qquad (4)$$

(Actually, any sample period $\tau = (2N+1)/4f_{IF}$, N=0,1,... will achieve the separation.) Since a single mixer and a single ADC produces both I and Q, the gains and phases of the two signals are guaranteed to be equal, apart from a time delay of one sample period. The ADC output stream is delivered to the digital filters which start by separating I and Q and reversing the sign of every other sample giving two time series at a sample interval 2τ ($=3/2f_{IF}$). In the implementation in the SWR-503 electronics, the I data are sampled a time τ after the Q data.

Ref. [2] gives other methods for deriving I and Q from the output of a single ADC that is sampling the modulated IF signal. In these approaches, f_{sample} is not restricted to 4/3 f_{IF}, but digital filters are required to extract I and Q from the ADC output.

The digital filters provide two stages of FIR filtering, with up to 128 coefficients in each stage, and with subsampling permitted after each stage. The digital filters perform three functions :

(a) Time-shifting so the I and Q time series refer to the same time;
(b) Low-pass filtering and subsampling to get a lower output data rate;
(c) Matched filtering (pulse compression).

In the measurements reported here, the first stage was used to do the time-shifting and low-pass filtering while the second stage did the matched filtering. The division of functions between stages is arbitrary and could be done in any order, or even by one stage if a single stage could provide enough coefficients.

The system then writes to a disk the filtered 16-bit I and Q data corresponding to the range bins specified by the user. After a run, the data were transferred from the disk to tape and were analyzed off-line. There was no provision for on-line monitoring or analysis of the data.

3.2.1 Data recorder limitation

The total rate at which the system can acquire data is limited by the rate at which the ADC's can run (<600 kHz in this case), the digital filter speed, and the rate at which the system can write data to the disk. For an 8-element array, with less than 64 coefficients in each stage of the digital filters, transfer to the disk provided the limit on data rate. Tests of the system showed that at a data rate of 820 kB/s, there were no disk-transfer errors, but at 980 kB/s, errors were common. Thus the overall performance of the system is limited by the existing data-recorder software and operating system which limit the data-acquisition rate to :

$$\text{(no. of channels)x(no. of range bins)x(pulse rate)} < 204800/\text{s} \ .$$

With an 8-element receive array, this meant that the pulse rate was restricted to 100/s with 256 range bins, 160/s with 160 range bins and 200/s with 128 range bins.

In order to examine high-Doppler shift targets, or to keep the duty cycle of the transmitters high with short pulses, a high pulse rate is required. In order to examine a broad span of target ranges, a large number of range bins is required. In order to maximize SNR by reducing the beam width of the array, the number of channels must be as large as possible. Thus the limit on the data-acquisition rate imposed by the existing data recorder is presently limiting the effectiveness of the portable radar.

Fixing this limitation will likely require replacing the operating system that controls the radar electronics, the software that stores that data, and the storage device itself.

3.3 Transmitter electronics

As configured for these tests, the radar transmits short binary-phase-coded pulses. The controlling computer reads a file containing the modulation envelope sampled at 6.2×10^5/s, and loads it into the pulse generator. On command from the timing control unit, the pulse generator creates a low-voltage (2 V_{pp}) pulse at the carrier frequency f_0 with the specified pulse shape.

3-, 7- and 11-bit Barker codes (Ref. [3]) with 25- and 40-μs bits were used for the measurements. It was found that sharp transitions in the waveform resulted in oscillations and noise in the transmitter output that lasted long after the pulse had ended, so the simple binary-coded waveforms were also smoothed with a 19-μs hanning window. This eliminated the ringing and reduced the output power by only 16% for the 25-μs-bit codes and 10% for 40-μs bits. It also had the effect of increasing the pulse length by 19 μs.

The output power was provided by four Analogic AN6028C power amplifiers, each capable of provided 2 kW (peak). A combiner was used to couple the outputs of the four amplifiers to the Heliax LDF4-50 antenna cable. The power amplifiers were equipped with meters indicating reflected power, and during operations they always indicated at least 6% reflected power. It is not known whether this indicates a mismatch in the combiner impedance or an error in the meters. It is not likely that the power was reflected from the antenna because other measurements indicated a good impedance match near 24.5 MHz (see Section 2.1 and Figure 4 above).

3.4 Mechanical and Electrical

The radar electronics, including air conditioners, are mounted in a 20-ft long trailer which has a total weight of 4500 lb.

The total power consumption of the electronics is 8.4 kW of which 6.4 kW is required for the transmitters. Lighting and test equipment require ~1 kW and 3.8 kW is required for each of the two air conditioners. Thus the minimum power consumption is 9.4 kW, and it rises to 17.0 kW when both air conditioners are in use.

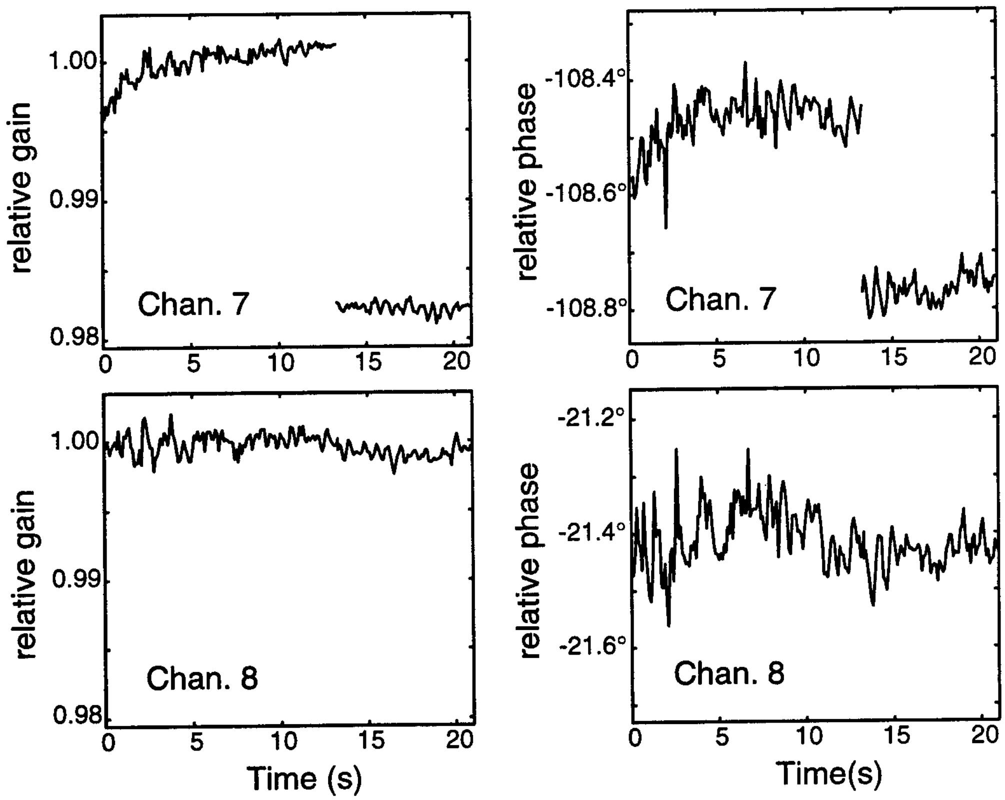

Figure 7. A gain jump in one channel of the radar. The gain jump occurred in <7.4 ms. The signal amplitudes were (i) averaged over each snapshot (256 points, 2.56 ms of data), (ii) divided by the amplitude in channel 6, and (iii) normalized to unity in the interval 0-13 s. The phases are relative to channel 6.

3.5 Electronics problems

The electronics worked well during the tests of the system, but a few problems were encountered. Most of them would not result in a serious degradation of the radar performance.

3.5.1 Receiver gain and phase jump

Figure 7 shows the relative amplitudes and phases of channels 7 and 8 in a data segment where a sharp jump in channel 7 was observed. In this measurement, a CW source was placed on the ground on the array boresight at a range of 285 m, only the receivers were operating, and the radar carrier frequency was set to 24.440 MHz while the source was tuned to 24.441 MHz. The source signal was ~50 dB greater than all other signals in the output. Data were recorded in 256-pt snapshots at a sample rate of 10^5/s (both I and Q), at a rate of 100 snapshots/s. Amplitudes and relative phases were averaged over one 256-point snapshot. The relative gains plotted in Figure 7 are the amplitudes in

channels 7 and 8 divided by the channel-6 amplitude and then normalized to an average value of 1 for time 0-13 s. The relative phase is the phase difference between the specified channel and channel 6. We attribute small fluctuations observed in the relative amplitudes and phases to antenna motion in the moderate wind that was blowing at the time. The jump in channel 7 appears in both the amplitude and phase. The gain change by a factor 0.984 is a reduction of 0.14 dB in signal power.

We can say very little about the origin of this gain jump. It happened suddenly : the jump occurred during the 7.4-ms period between the end of one snapshot and the start of the next. If it is due to a poor cable connection to the antenna, a resistance of 0.8 Ω or an inductance of 60 nH must have appeared in series with the antenna impedance of approximately $50+j0\ \Omega$. More likely, an active element in the receivers changed abruptly.

It is hard to say whether gain jumps like the one displayed in Figure 7 are serious. For most signals a gain change of 0.14 dB is insignificant compared to the system noise. Gain stability is probably most important if we wish to observe nearby targets in the presence of strong ground returns, where a small change in the received amplitude due to a gain change could be as significant as the target echo.

It is not known how often gain jumps occur. Gain changes of ~0.1 dB and phase shifts 0f ~0.2° are detectable only when measuring a strong constant-amplitude source, and we took only ~100 s of such data during the test program in 1998.

3.5.2 Data dropouts

For several runs, the *I* component from one of the channels was missing (i.e. always 0). This was later traced to a poor connector on one of the digital-filter units. The problem is worth noting principally because the controlling software does not notice the absence of useful data, and we had no method of detecting the condition of the electronics in real time. As a result, the failure was only discovered later when the data were being analyzed. The appearance of this problem indicates the need for a real-time ability to look at short samples of data.

The problem never reappeared after the digital filter unit was replaced.

3.5.3 Pulse generator errors

An intermittent, but recurring, problem with the system was reduced amplitude in the output of the waveform generator. The symptom was that the pulse being fed to the transmitter amplifiers would drop from its nominal amplitude of 2 V_{pp} into 50 Ω (the maximum observed was 1.98 V_{pp}) as low as 1.34 V_{pp}. As far as could be determined, the pulse shape was not affected.

The source of the problem was never isolated. In radar operations it will appear as a drop in peak output power which is indicated on a meter on the Analogic AN6082C power amplifiers, so there should be no risk that a major reduction it would go unnoticed during experiments.

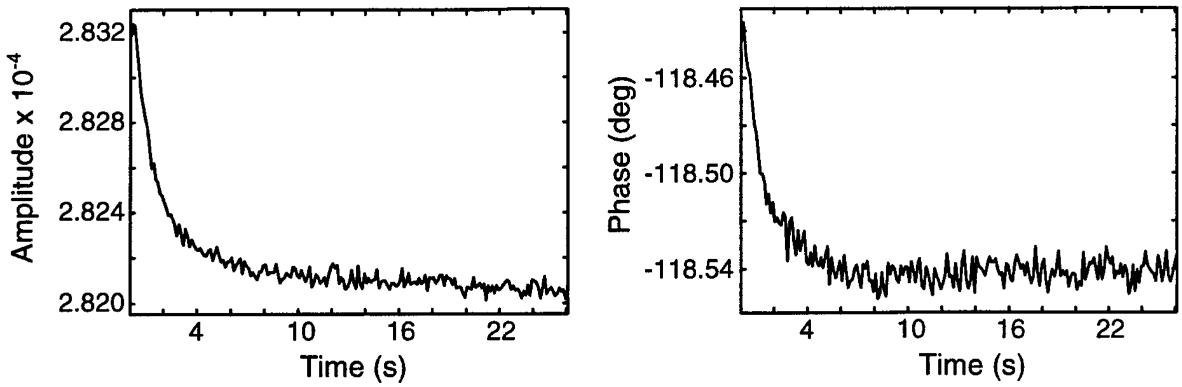

Figure 8. The amplitude in one channel during a loopback run. The amplitude is the square root of the sum of I^2+Q^2 in the output time series. All channels showed the same behaviour.

A small amplitude and phase drift was observed in the waveform generator output during loopback experiments in which the output of the pulse generator was attenuated and then fed directly to the receiver inputs, bypassing the transmitters, cables, and antennas. This resulted in a huge signal that overwhelmed all noise in the system and made it possible to detect tiny amplitude and phase variations in the outputs. Figure 8 shows what always happened during loopback runs : over a period of ~10 s, the signal amplitude in all channels dropped by 0.5% (0.04 dB) and the phase shifted by ~0.10°. Because it happened in all channels, and is associated with turning on the pulse generator, we attribute it to the pulse generator. It is not known why this happened. Clearly it is related to the fact that the waveform generator is dissipating power, but the signals in the waveform generator are only a few volts into 50 Ω, so power levels should be ≤100 mW and currents <100 mA. One would not expect this to have any noticeable effect on the electronics.

This small drift will have no effect on target detection.

3.5.4 50-MHz-clock dropouts

Figure 9 shows the phase measured during one of the loopback runs. The sharp jumps in phase last for only one pulse, and amount to a jump of 2.2°. This is explained as a timing error in which one cycle is missing in the 50-MHz controlling signal. Consequently, there is a time delay of 20 ns and a phase shift of 2.16° in the 300-kHz IF signal.

These dropouts do not affect the relative phases of the channels, or the signal amplitudes. In the worst case, the effect of the dropouts on a narrow-band signal would be to add a noise signal with a relative strength of -39 dB. In other words, isolated dropouts are a nuisance when plotting figures, but they have almost no effect on the operation of the system.

The real problem is that the amplitude of one of the oscillator outputs may be too low, and the system may be close to not operating at all.

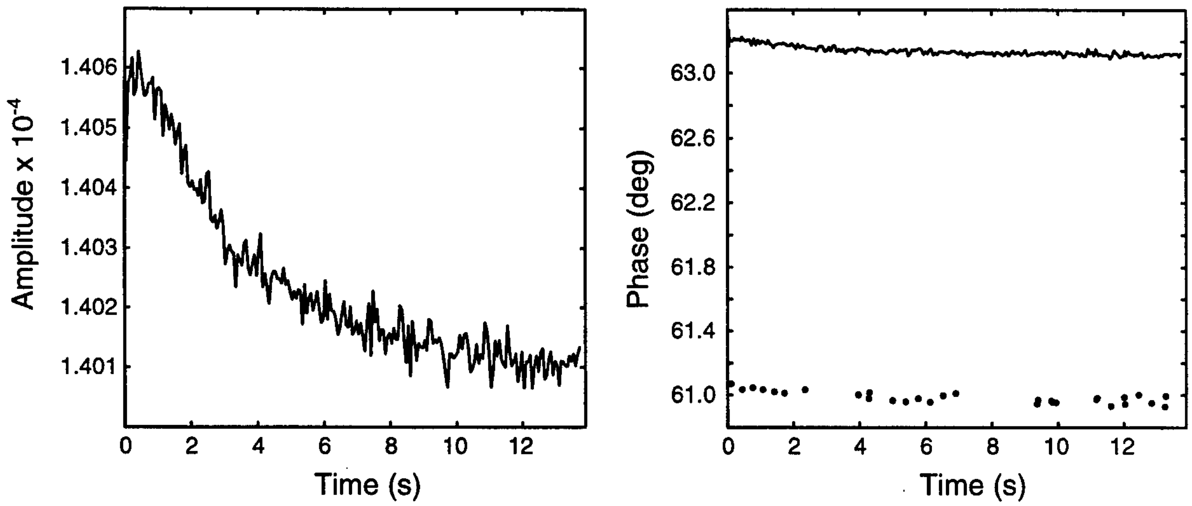

Figure 9. One channel during a loopback run showing the 2.16° phase jumps resulting from missing one cycle of the 50-MHz oscillator. All channels displayed the same phase jumps.

3.5.5 Imperfect *I* and *Q* matching.

Raytheon Canada's HF radar separates the *I* and *Q* components of the received signals by sampling the IF signal at $4/3 \times f_{IF}$ using a single ADC (see Section 3.2 above). This is supposed to guarantee that the phases and gains of the two components are matched exactly. In fact this did not happen with the receivers tested here.

The *I/Q* mismatch appeared most clearly in loopback experiments in which the waveform-generator output was attenuated and then fed to the receivers, but it was also detected with strong radar echoes. This subsection describes the analysis of one loopback experiment in which the modulation waveform was a simple 50-μs pulse with 19-μs hanning tapering. The 1.97-V_{pp} output pulse was fed through a 50-dB attenuator and an 8-way splitter to the receiver inputs. The ADC sampling rate was 400 kHz ($\leftrightarrow f_{IF}$=300 kHz), the digital filter consisted of a single-stage 16-tap low-pass anti-aliasing filter (i.e. covering 80 μs of data) with a cutoff frequency of 37.9 kHz, and after subsampling, *I* and *Q* data were recorded at a rate of 100 kHz. A basic sampling rate of 200 kHz means that power in the 180-220 kHz range is aliased to the 0-20 kHz band in the sampled *I* and *Q* spectra, but aliasing was not a problem since the receiver bandpass is only ±50- kHz and, with the smoothed pulse shape used in this loopback run, the power is reduced by >70 dB at frequencies above 180 kHz. As discussed above, the *Q* data sampled by the ADC are delayed by 1 ADC sample interval(=2.5 μs) relative to the *I* data. The digital filter was designed to advance the low-frequency *Q* data by 1/2 ADC sample interval and to delay the *I* data by the same amount, and to have the same power transfer function for both channels. (This was achieved by reversing the *Q*-filter coefficients to get the *I*-filter. Digital-filter design is discussed in Section 4 of this report). The data considered here are the

average of 480 pulses acquired between 8.0 and 10.4 s after the start of the run (the 8-s delay avoided the pulse-generator drift at startup (see Section 3.5.3 above)). The signal exceeded the noise in the averaged data by more than 75 dB.

Figures 10-13 are four different plots of the same I/Q mismatch in channels 2 and 7 of the 8-channel system. The other channels displayed similar errors. Figure 10 shows the I and Q signals normalized so that

$$\sum I_k^2 = \sum Q_k^2 = 1 \quad .$$

and with the sign changed where necessary so the plotted pulses are positive. Examination of these figures shows that Q lags I in channel 2 but Q leads I in channel 7, and that the Q and I signals have slightly different shapes. If the pulse produced by the waveform generator is just the carrier frequency multiplied by a real envelope $S(t)$, then I and Q should be $S(t)$ multiplied by phase factors and a real gain α :

$$I(t) = \alpha\cos(\Phi)S(t) \quad ; \quad Q(t) = \alpha\sin(\Phi)S(t) \tag{5}$$

With the normalization used in Figure 10, the plots of I and Q should be exactly the same.

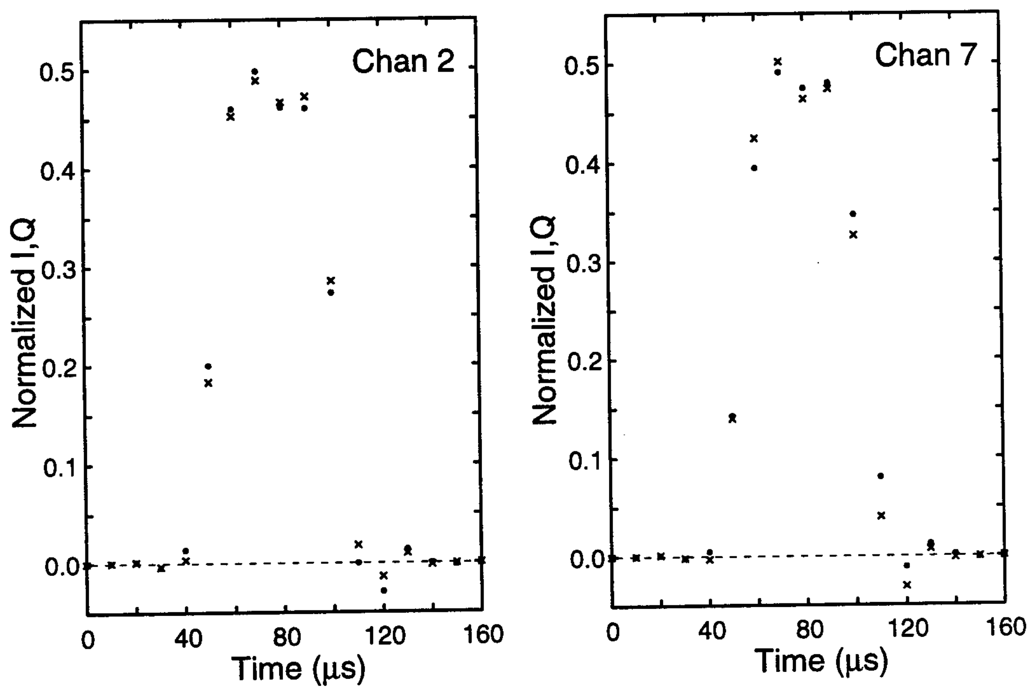

Figure 10. Plot of normalized I and Q in a loopback run using a simple 50-μs pulse with a 19-μs hanning taper showing the different pulse shape for I and Q and for channels 2 and 7. The data plotted are the average of 480 pulses. The signals are normalized so $\Sigma I^2 = \Sigma Q^2 = 1$. Dots : I Crosses : Q.

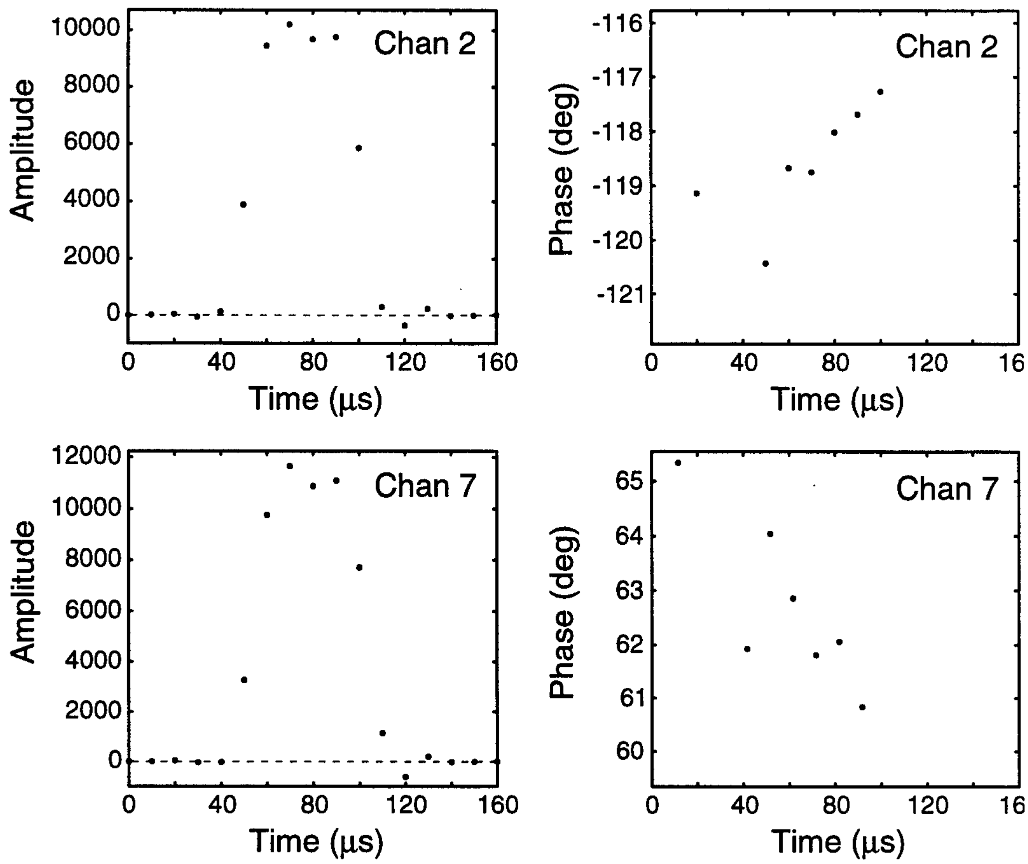

Figure 11. The amplitude and phase in channels 2 and 7 in the loopback data. See eq.(3a,b) for the definition of amplitude and phase.

Figure 11 displays the amplitude and phase of the signals. The phase is

$$\Phi(t) = \arctan[Q(t) / I(t)] \tag{6a}$$

and the amplitude is

$$A(t) = \sqrt{I^2 + Q^2} \times \cos[\Phi(t) - \Phi(70\mu s)] \quad . \tag{6b}$$

This definition of amplitude allows Figure 11 to show where I and Q changed sign. The variation in phase illustrates one major consequence of the I/Q mismatch : namely, it is hard to attach much meaning to the relative phases of channels at a level better than about ±2°.

Figure 12 shows the power spectra calculated separately for I and Q. The deep minima at 20 and 40 kHz are expected for a smoothed 50-μs pulse, but note that there is a significant difference in the shape of the minima in the I and Q spectra. We have no idea why the I signal lacked the very deep minima displayed by Q.

Finally Figure 13 displays the amplitude ratio R and the I-Q phase delay $\Delta\tau$

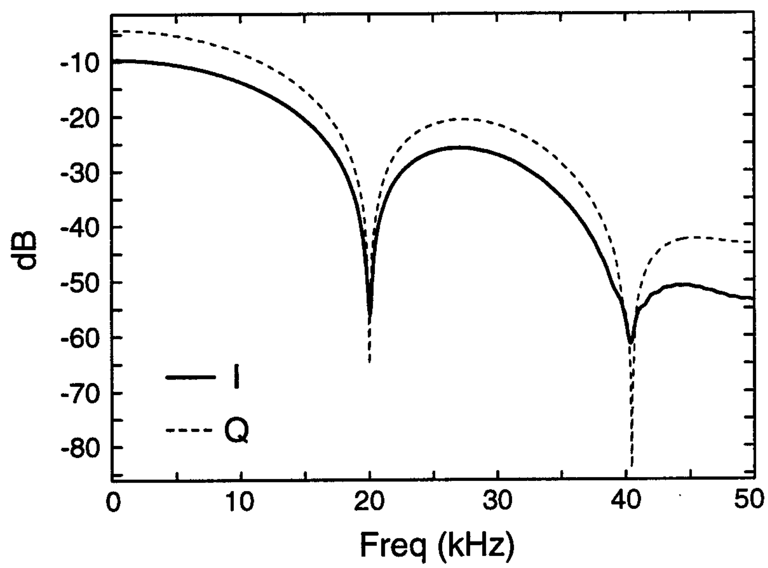

Figure 12. The power spectra of the I and Q signal averaged over 480 loopback pulses. The ADC quantization noise for a 480-pulse average sampled at 10^5/s is –84.6 dB.

$$R(f) = \frac{|I(f)|}{|Q(f)|} \quad ; \quad \Delta\tau(f) = \frac{\Phi_Q(f) - \Phi_I(f)}{2\pi f} \tag{7}$$

where $I(f)$, $Q(f)$ are the Fourier Transforms of $I(t)$, $Q(t)$, and $\Phi_I(f)$, $\Phi_Q(f)$ are the phases of $I(f)$, $Q(f)$. In an ideal system, where eq.(5) holds, $R(f)$ is independent of frequency and $|\Delta\tau(f)|=0$. The I-Q phase delay due to the low-pass digital filter is $|\Delta\tau(f)|<2$ ns for $f\leq 40$ kHz, so essentially none of the delay shown in Figure 13 is due to the filters. Further, there is a delay of the same magnitude (~1 μs↔0.1 range bin) between channels (not shown in Figure 13).

Beyond plotting the data, there is little to say about this I,Q mismatch. The data do not indicate the origin of the error, beyond the fact that it must originate in the receivers since there are differences among the receiver channels. Figure 11 shows that the phase varies by ~1° in 10 μs, and Figure 13 shows that, for f<15 kHz, the mismatch can be modeled approximately as delay of Q relative to I. Errors of this magnitude will not have a significant effect on estimates of range, Doppler shifts, and bearing angle.

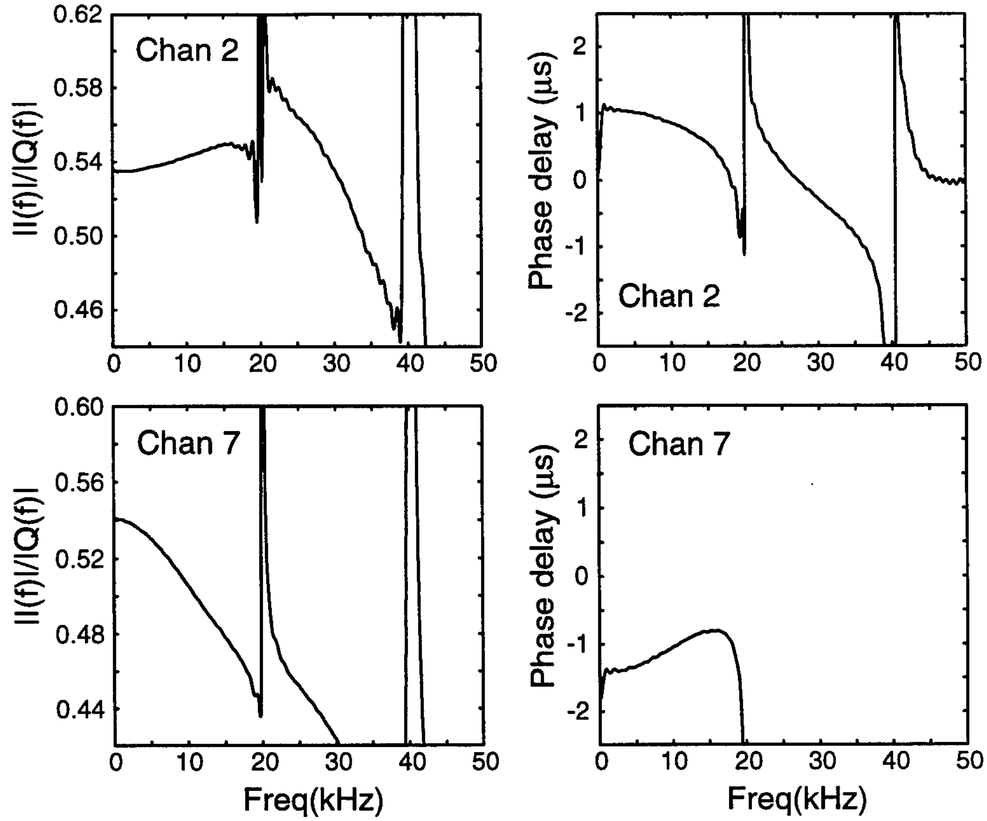

Figure 13. The amplitude ratio for I and Q and the phase delay of Q relative to I for channels 2 and 7 in the average loopback data. I(f) and Q(f) are the Fourier transforms of I and Q.

The source of this error should be understood principally to verify that it is not a symptom of other problems in the receiver electronics.

4. Digital Filter Design

The digital filters incorporated in the radar system (see Figure 6 and Section 3.2) perform three functions :

(a) low-pass filtering to remove high-frequency noise before decimation to lower sample rates;

(b) time shifting I and Q to remove the time difference of 1 ADC sample interval;

(c) pulse compression (matched filtering).

These functions could be performed by a single-stage filter, but the radar used here had 2 stages of digital FIR filters with the option of decimation after each stage. It was found to be convenient to have the first stage do the low-pass filtering and time shifting, while the second stage filter did the pulse compression with a filter matched to the pulse shape. This division also made it easy to operate the system with a low-pass filter but no matched filter.

4.1 Low-pass, time-shifting filters.

The low-pass, time shifting filters were designed in a very simple way . Let g_n and h_n, n=0,...,N-1, be the coefficients of the I and Q filters so the outputs of the first-stage filters are :

$$\hat{I}_k = \sum_{n=0}^{N-1} g_n I_{k-n} \quad ; \quad \hat{Q}_k = \sum_{n=0}^{N-1} h_n Q_{k-n} \quad . \tag{8}$$

The filters must be designed so the power transfer functions for I and Q are identical and the time delay of I is 1 sampling interval greater than the time delay of Q.

Restricting the filters to the form :

$$h_{N-1-n} = g_n \tag{9}$$

satisfies the power-transfer constraint and ensures that, if the phase delay of I at frequency f is N-1/2+$\delta(f)$ samples, then the phase delay of Q is N-1/2-$\delta(f)$. The design goal is $\delta(f)$ =1/2. The phase-delay error in ADC-sample periods is :

$$\text{phase-delay error} = 2\delta(f) - 1 \tag{10}$$

We would also like the filters to have linear phase (i.e. phase and group delays independent of frequency), at least at low frequencies. As long as

$$g_{N-1-n} \cong g_n \quad ; \quad h_{N-1-n} \cong h_n$$

then the filters will have nearly the same phase delay at all frequencies. This condition means that the filters are nearly-even functions.

To design N-point low-pass filters for I and Q (each with sample rate = 200 kHz = 2/3f_{IF}), a $2N$-point low-pass filter for a 400-kHz sample rate was designed by the windowing method (Ref. [4])

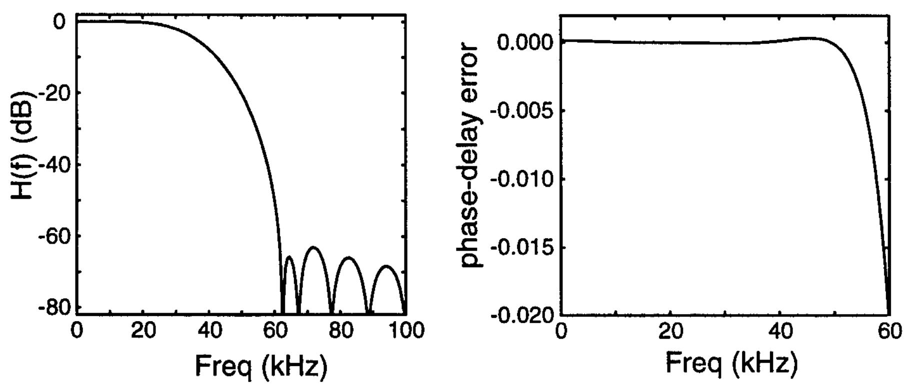

Figure 14. The characteristics of a 16-point I/Q matching filter designed for a 400-kHz ADC sample rate. Left : Power transfer function (dB). The 6-dB cutoff frequency is 37.8 kHz. Right : The phase-delay error in ADC-sample periods(= $2\delta(f)$-1; see eq.(10)).

using MATLAB. Then the I and Q filters were given by the coefficients F_k of the $2N$-pt 400-kHz filter :

$$g_k = F_{2k+1} \quad ; \quad h_k = F_{2k} \quad ; \quad k = 0,\ldots,N-1 \tag{11}$$

Since $F_{2N-1-k}=F_k$, these I and Q filters have the same power transfer function. The parameters of the windowed filter (cutoff frequency and windowing function) were varied to get filters with the minimum phase-delay error (see eq.(10)).

Figure 14 is an example of the results that were obtained. In this case, the object was to get a cutoff frequency ~40 kHz so that the I and Q data could be decimated to a sample rate of 100 kHz before being stored on the disk. The filter length is N=16 (80 μs). The filter was designed as a 32-pt filter with a 6-dB cutoff frequency of 37.844 kHz (f_{sample}=400 kHz) using Chebyschev windowing with a 50-dB ripple parameter. This simple approach gives nearly-perfect I/Q matching throughout the passband of the filter.

In the radar measurements described in this report, the transmitted pulse never had significant power above 40 kHz, and in addition the receiver's pass band was only ±50 kHz, so low-pass filtering followed by decimation of I and Q was always performed and the procedure described here was very convenient. In fact, low-pass filtering may not have been necessary because the crystal filters in the receivers had already band-limited the signals.

An alternate procedure would be to time-shift the I and Q data using the methods given by Ref. [5], and then, if required, apply the same low-pass filter to the time-shifted I and Q. Because of the relation between the ADC sample rate and f_{IF}, in no case are complicated filters required to complete the separation and time-matching of I and Q (Ref. [2]).

The value of perfect I/Q matching filters with delays $\delta(I)=-\delta(Q)=1/2$ must be questioned in light of the phase and amplitude errors shown in Section 3.5. In the future, it may make more sense to use the first FIR stage to provide a different time shift for I and Q of each receiver, so that all signals are

time-matched entering the second stage of the digital filter. Low-pass filtering and matched filtering would be done in the second stage.

4.2 Matched filters for pulse compression

As operated in the measurements described here, the transmitted pulse was a simple binary-phase coded signal. The appropriate 2nd-stage matched filter for pulse compression then was just the transmit pulse shape, filtered with the 1st-stage low-pass filters. Because it was assumed that I and Q were time-shifted before entering the second stage of the digital filters, they used the same matched filters.

In a few measurements, the stage-2 matched filter was not used. This was done in situations, such as the loopback measurement discussed in Section 3.5 above, where the measurements were intended to examine details of the receiver output, rather than measure delay time of a replica of the transmitted pulse.

5. Calibrations

A full calibration of the radar system would require measurements of

(i) the radiation patterns of the antennas,

(ii) the transmitted power, and

(iii) the absolute gain and relative phase of the receive-array channels.

In the work reported here, only part (iii) of the calibration was done. This is the most important part of the calibration of the system because knowledge of the absolute gain allows the noise levels of the system and environment to be measured and beamforming can be done if the relative gains and phases are known.

As discussed in Section 2.2 above, at HF it is difficult to measure the far-field radiation pattern of an antenna. Since NEC gives physically-accurate results, it was decided to use NEC calculations rather than to attempt to measure the patterns. In any case, measurements are probably less accurate than the NEC calculations of the radiation patterns, even taking into account the error in the calculations due to uncertainty in the ground permittivity and conductivity.

The actual transmitted power was not measured. However, the peak output of the transmitters is known (2 kW from each of four modules), the amplifiers had meters indicating low reflected power (~6%), and measurements showed that the antenna impedance was nearly $50+j0\ \Omega$ near 24.5 MHz. The manufacturer's specifications show that the attenuation in the 100-m transmitter cable is ~1.1 dB. Thus, the peak transmitter power is ~5.8 kW.

This section discusses the determination of absolute receiver gain from loopback measurements, and the measurement of relative gains and phases using a nearby source and meteor echoes.

Table I. Sensitivity, receiver noise and total noise for the 8-channel portable HF radar. The external noise is the difference between the total and receiver noises. All measurements are referred to the receiver inputs. Inorder to refer the noise power to the antennas, the cable attenuation of 3.5 dB must be added to these values.

Channel	Sensitivity (nV/ADC step) run TK	Receiver noise dBW/Hz Run RB	Total noise dBW/Hz Run VW	External noise dBW/Hz
1	126	-184.9	-182.6	-186.5
2	117	-184.9	-182.8	-187.0
3	113	-185.4	-183.6	-188.1
4	138	-184.0	-181.7	-185.4
5	116	-185.5	-183.5	-187.9
6	118	-185.4	-183.5	-188.1
7	105	-185.6	-182.2	-184.9
8	109	-185.0	-181.6	-184.2

5.1 Absolute receiver/ADC gain and system noise.

The receiver/ADC gain was measured in loopback runs in which a simple pulse shape that included a 50-μs constant-amplitude segment was fed from the waveform generator through a 50-dB attenuator and an 8-way splitter to the receiver inputs. The first-stage digital filter was a 38-kHz low-pass filter as described in Section 4.1 above, there was no stage-2 matched filter, and the amplitude was measured toward the end of the 50-μs segment so that the filter ringing had decayed. The results are listed in Table I. With the sensitivities shown, the ADC quantization noise at a sample rate of 200 kHz is 1.0×10^{-10}V(rms)/$\sqrt{}$Hz. (-217 dBW/Hz) which is 13 dB below the thermal noise level of -204 dBW/Hz.

The combined receiver/ADC noise was measured by placing 50-Ω terminators on the receiver inputs and again running with the same digital filters. The power spectra of the noise data were examined to verify that the noise was nearly white, and to determine the white-noise floor of the system.

Figure 15 shows noise spectra of channel 2 with the 50-Ω terminator on the input and also with the antennas connected, but with the transmitters off, at a quiet time of the day; the other channels showed the same spectral characteristics. With the terminated input, the noise is not exactly white, rising from –185.15 to –184.47 dB between –22 kHz and +22 kHz, and electronics effects create weak spectral lines at multiples of 20 kHz (I,Q sample rate/10). Table I lists the total receiver/ADC noise for all 8 channels determined from power spectra like the one shown in Figure 15.

Figure 15 also shows the noise with the antenna connected, at the quietest time of the day (02:00 EST). It is not known why the electronics-generated signal at –40 kHz is so strong in this

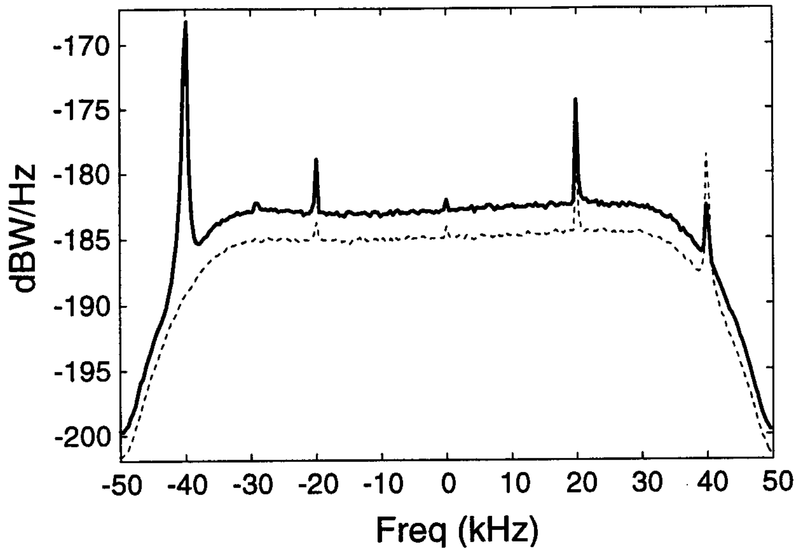

Figure 15. Noise spectra for receiver-channel 2 referred to the receiver input. Dashed line : 50-Ω terminator on receiver input. Solid line : Total noise with antennas attached at quiet time of day (02:00 EST). The lines at multiples of 20 kHz are due to radar electronics. The spectra were calculated by the Fourier Transform method with a frequency-bin width of δf=391 Hz.

spectrum (and in the spectra of the other channels). Table I lists the total noise powers at the receiver input with the antennas connected, and also the "external noise"(the difference between the noise powers with and without the antennas). Since the 100-m RG213 coaxial cables connecting the antennas to the electronics attenuated the signals by 3.5 dB, the noise powers referred to the antennas are 3.5 dB higher than those listed in Table I.

The external noises of the different channels should be the same, but the results listed in Table I vary over a range of 4 dB. We have no explanation for this. The antennas and cables were identical so there should have been no significant difference. NEC estimates of antenna coupling, discussed in Section 2, show that there should be no gain variation of this magnitude.

At the quiet time of the day, the external noise is ~2 dB below the receiver noise. A preamplifier with a gain of ~8 dB and a noise figure <15 dB would be required to eliminate the receiver self-noise as a significant factor in the system performance.

5.2 Transmitter OFF-state noise

In a monostatic radar such as the portable HF radar, the transmitters are turned off during the period in which signals are being received. Since the transmit antenna is close to the receive array (20-60 m separation in the tests in 1998), low-noise operation requires that the amplifiers drive no noise to the transmit antenna while the receivers are enabled.

The direct transmission of noise from the transmitter to the receivers (the "OFF-state noise") was measured by comparing Doppler noise spectra measured in two runs recorded during a low-external-

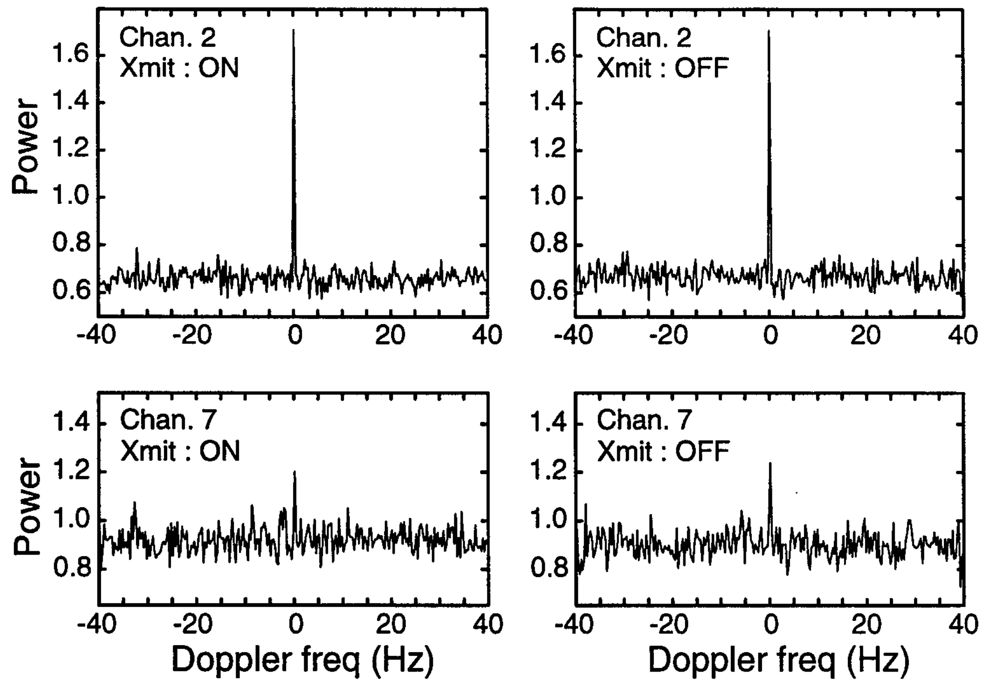

Figure 16 Doppler spectra measured with the transmitters on and off.
Left : Transmitters ON (radar run). Right : Transmitters OFF (noise run)
Top : Array channel 2 Bottom : Array channel 7
The spectral power is given in (ADC step)^2/Hz and is not corrected for attenuation by the digital filters.

noise time of day (01:35 to 01:48 local time). The first run was a radar run with a peak transmitter-amplifier output of 8 kW (~6 kW broadcast), a pulse rate of 80/s, and a 7-bit Barker code with 25-μs bits giving an average radiated power of ~80 W. The second run, recorded a few minutes later, had exactly the same setup parameters (digital filters and pulse rate), but the transmitter amplifiers were disabled by turning off their main 208-V power supplies. Figure 16 compares Doppler spectra calculated for two receiver channels in the two runs. In both cases, 4096 pulses (=51.2 s of data) from 50 consecutive range bins was analyzed. The Doppler spectra shown were averaged over the range bins and then smoothed in frequency to get a bin width δf=0.31 Hz (i.e. each spectrum bin is an average of 800 power estimates). The range bins used covered target ranges 76 to 150 km because meteor reflections appeared only at greater distances.

Comparison of the left and right columns in Figure 16 shows that there is no significant difference in the Doppler noise spectra between the two runs, and we conclude that there is negligible contribution to the system noise by direct interference from the transmitters to the receivers. Analysis of the spectra shows that, except at f=0, having the transmitters on increases the noise <0.07 dB. In the f=0 bin of the unsmoothed spectra, (i.e. –0.0098 Hz<f<0.0098 Hz) of both of the channels plotted in Figure 16, the signal is 0.6 dB higher when the transmitters are on. This indicates that the transmitters are creating a weak interference that is synchronized with the pulse generation.

We conclude that the OFF-state noise of the transmitters is negligible.

Table II. Relative amplitudes and phases for measurements of a source placed at a standard position on three different days. The run-to-run variations are much greater than the statistical errors due to system noise. Positive relative phase means a signal leads channel 1.

Channel	Relative amplitude			Relative phase		
	28 Oct. 98	30 Oct. 98	3 Nov. 98	28 Oct. 98	30 Oct. 98	3 Nov. 98
1	1	1	1	0	0	0
2	0.9906	0.9910	1.0046	21.18°	20.61°	21.13°
3	0.9719	0.9713	0.9909	37.41°	36.86°	36.80°
4	0.8177	0.8202	0.8343	55.18°	54.06°	54.20°
5	1.0426	1.0330	1.0514	-129.97°	-129.91°	-129.98°
6	1.0079	1.0043	1.0211	-126.93°	-127.33°	-127.20°
7	1.2435	1.2340	1.2748	-128.48°	-129.67°	-128.44°
8	1.0552	1.0486	1.0730	34.29°	33.40°	33.80°

5.3 Relative gains and phases measured using a nearby source

The measurement of the relative gains and phases of the 8 elements of the receive array initially was done using a low-power transmitter which was placed ~25 λ in front of the receive array (i.e. in the far field). The purpose of these measurement was twofold :

(i) By making repeated measurements of the relative responses with the source in one position, it would be possible to verify the stability of the relative gains and phases.

(ii) It would provide a relative calibration for the array.

The first concern arose because another group using the same electronics in late 1996 had reported phase shifts that they could not explain. The source was a low-power CW transmitter mounted in a small aluminum box with a short (1 m) vertical whip antenna. The CW source was tuned to 24.441 MHz while the radar receivers were operated at a carrier frequency of 24.440 MHz. Care was taken to ensure that the source did not overload the receiver channels.

Table II lists the results of 3 measurements of the relative gains and phases taken with the source placed at the same position (within 2° of boresight, ~285 m from the array) on 3 different days. There are variations of ~ ±1% in the relative gains and ~0.5° in the relative phases. These changes will have no significant impact on the ability to do beamforming with the receive array, and it is concluded that there is no evidence for gain and phase instability with these electronics.

The origin of the small variations is not known, but they are not random statistical fluctuations due to noise in the electronics. Probably they are due to changes in the antenna gains, and in the propagation of the 24.44 MHz radiation, perhaps due to changes in ground moisture. The antennas were able to turn slightly when the wind blew, and this may have turned them by as much as 2°.

Table III. Summary of the relative amplitude and phase measurements with a source at 285 m from the array on the boresight and 29° to the right. The relative amplitudes and phases are normalized by a loopback measurement to remove the effects of receiver gains and phases. The source distance is only 7×(array size), so corrections have been applied to account for the different source-to-element ranges and different antenna gains. The relative amplitudes are normalized so $\Sigma(\text{rel.amplitude}_k)^2=8$. *A linear fit was done to the relative phases, and the fit errors are listed in the table. The bottom row of the table shows the source directions estimated from the linear fit to the relative phases.*

Channel	Relative amplitude		Phase error = Corrected phases – linear fit	
	α=0±1°	α=-29±1°	α=0±1°	α=-29±1°
1	1.0440	1.2875	-7.67	-3.20
2	0.9655	1.1475	2.03	-0.07
3	0.9700	1.0297	4.73	-0.12
4	0.9451	0.9377	3.62	0.68
5	1.0106	0.8455	-0.94	-0.22
6	0.9928	0.9157	-2.26	9.70
7	1.0977	0.9976	10.71	1.96
8	0.9656	0.7330	-10.22	-8.73
			Fit α=1.5°	Fit α=-28.5°

In a second part of the source measurements, the source was placed at 29±1° to the right of the boresight direction at a distance of ~285 m. It was hoped that this measurement would verify that the relative phases and gains measured with the source on the boresight would also describe the system's response at other angles, apart from a relative phase at element n of $(n-1)kd\sin\alpha$ radians where d is the element spacing in the linear receive array and α is the angle to the left of the boresight (see Figure 5 and the discussion in Section 2.3) . The comparison of the boresight (α=0±1°) and the α=-29±1° measurements is displayed in Table III.

NEC modeling of the 8-element array (Figure 5) shows that, for angles within ~40° of the boresight, the relative gains and phases of elements 2-7 should lie in the range 1±0.03 and 0°±2° respectively. Only elements 1 and 8 should show any significant coupling effects, with phase errors of -6° on boresight, and relative gains of ~1.08 (element 1) and 0.88 (element 8) when α=-29°. The variations in the phase errors listed in Table III are much larger than this.

What is the source of this variation? Repeated measurements of the electronics showed that the relative gains and relative phases of the receivers were stable to a small fraction of the phase errors shown in Table III, and repeated measurements of the source at a single position (Table II) shows that variations in the source position and day-to-day variations in propagation can explain amplitude variations of <1% and <0.6° respectively. Finally, note that there is nothing consistent about the variations at α=0° and α=-29°.

The conclusion that can be drawn from these data is that variations in relative gains and phases are due to spatial variations in ground conductivity, and/or scattering from nearby reflectors. Whether the problem is variations within ~λ(=12 m) of the source, or ~λ of the antennas, or a general variation on the scale of the antenna-source distance (~300 m) cannot be determined from these results. In spite of this variability of ~10% in amplitude and 5° in phase, beamforming is still possible, and accurate source directions can be deduced from the array. However, this variability will degrade the ability to use beamforming to separate weak targets in one direction relative to strong targets in another.

Because these results showed that the array had a strong dependence on local propagation, it was decided to try to use meteor reflections to determine an angle-dependent calibration of the array. This is discussed in the next subsection.

5.4 Calibrations using meteor reflections.

The study of meteors using HF radar is an old science, dating from the late 1940's (Ref. [6]). When a meteor enters the Earth's atmosphere, it creates an ionized trail which reflects radar signals when the radar carrier frequency is below or comparable to the plasma frequency. The trails generally appear at altitudes of 80-110 km. After the trails are formed, the electrons diffuse and recombine so the reflections disappear after a period of 0.1-20 s.

For the radar data recorded and analyzed in the tests of the portable HF radar, data were recorded for target ranges of 30 to 410 km. The object of the meteor analysis was to calibrate the receive array, so it was necessary to ensure that the meteors appeared at an angle of 10°-20° above the horizon (i.e. in the main beam of the antennas). This meant that meteors at ranges >220 km were suitable for calibration.

Meteor trails are quite long, but they still appear as small reflectors. The first Fresnel zone for perpendicular reflection of radiation with wavelength λ from a meteor trail at a distance R_0 is a segment with length

$$\xi_1 = \sqrt{R_0 \lambda}$$

centred at the point of perpendicular incidence (the first Fresnel zone is the central part of the track where the reflections add in phase). Outside the first Fresnel zone the reflections add destructively, as long as the electron density varies slowly. Consequently, at the receive antenna, the source appears to cover an angle of only

$$\theta_1 = \xi_1 / R_0 = \sqrt{\lambda / R_0}$$

For a track distance R_0=220 km and a wavelength λ=12.2 m, the source covers only θ_1=0.4° which is effectively a point source for the 42-m-aperture receive array used here. After the ionized track is created, high-altitude winds blow parts of the track in different directions, and other nearby parts may

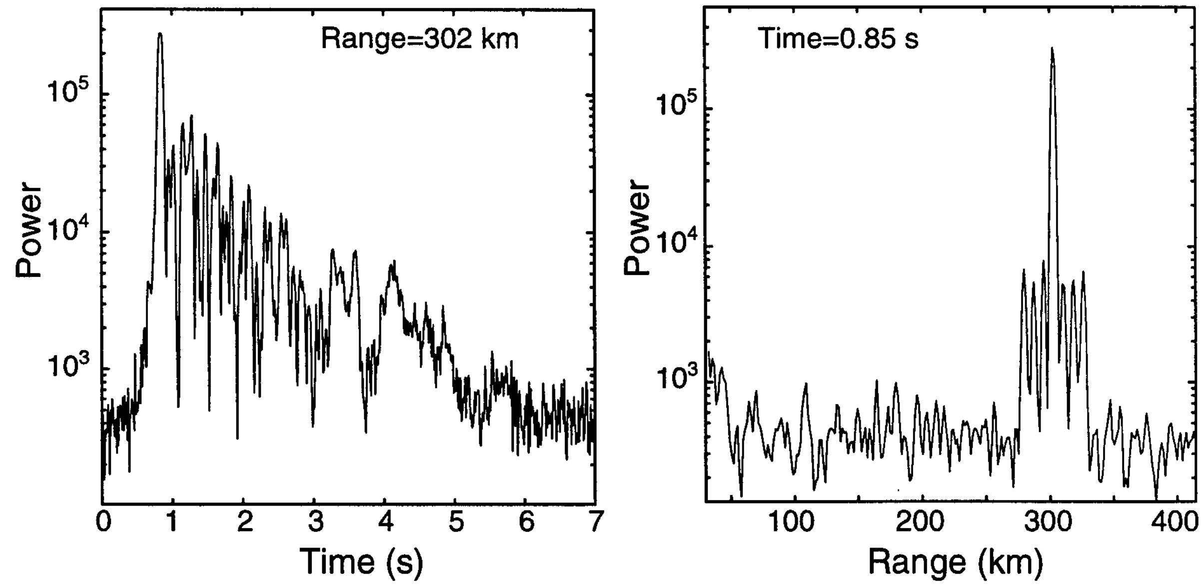

Figure 17. A typical meteor reflection. The received power is the sum of powers in the 8 channels of the receive array normalized by the relative gains measured in a loopback run. The transmitted pulses is a 7-bit Barker code giving 3 range sidelobes on each side of the main reflection.

begin to satisfy the Fresnel criterion, so it is expected that the apparent source size could increase to a few times θ_1. This would still be a point source for calibration purposes.

Figure 17 shows a typical meteor reflection from an overdense meteor track. The characteristics are the sharp rise time (<0.2 s), the fluctuating signal intensity, the relatively slow decay, and the narrow band of ranges over which the reflection occurs. The sharp rise occurs because the track is almost invisible until part of it is perpendicular to the line of sight to the radar (i.e. until it reaches its closest approach point), and after that time the signal is dominated by reflections from the part near the closest approach (the first Fresnel zone). As noted above, high-altitude winds distort the track, and interference occurs between reflections from different parts of the track. This results in fluctuations in the total signal intensity. The slow decay is due to electron diffusion and recombination which reduce the strength of the reflected signals. The decay times vary from ~10 s at 80 km altitude to ~0.1 s at 110 km. In the example shown in Figure 17, the transmitted pulse was a 7-bit Barker code with 25-μs bits. This resulted in three range sidelobes on each side of the main reflection.

The analysis of the meteor data was straightforward because only strong meteor reflections were used. The segments of data were specified as a set of pulses and range bins. For each segment, the received signals were first normalized using relative gains and phases computed from loopback runs and then a small time shift was done to align the reflections in different channels and to cancel the *I/Q* mismatch discussed above in Section 3.5.5. Then the relative amplitudes and phases of the receive-array elements were calculated for each pulse and range bin in the data segments. Finally the results from different pulses and range bins were combined in a weighted average. This gave one set of relative gains and phases for each segment of data. In the calibration performed on the portable HF radar, 85 segments of meteor data were analyzed. We refer to "segments of data" rather than tracks

because some of the tracks were analyzed as up to 4 segments in order to verify that different parts of the same track gave the same results.

To complete the calibration of the array, all 85 sets of relative gains and phases were analyzed simultaneously to determine

(i) The phase change per array element in each set. This is just the slope of a linear fit to the relative phases after subtraction of the estimated phase error for each element, and it gives the bearing direction for the meteor.

(ii) The average phase error in each element of the array. This is the difference, averaged over all the data sets, between the measured phases and the linear fits.

(iii) The phase error in each element in each set. This is the difference between the measured phase and the sum of the linear fit to a set and the average phase error for the array element.

Since the average errors are estimated from the linear fits, and the linear fits require an estimate of the average phase errors, the analysis had to be done iteratively. It was found that 2 iterations were sufficient for these data where the phase errors were small (<20°). It is not clear that this approach would work in a case where the phase errors were large.

The calibration procedure was carried out for all 8 elements for data sets 1-76, but channel 8 of the receive array was not operating for data sets 77-85. To determine the phases errors for data sets 77-85, a 7-channel analysis of all 85 data sets was done, and then the results were used only for the last 9 data sets.

The results of the calibration are displayed in Figure 18, Table IV lists the average phase offsets and Figure 19 shows the ranges and bearings of the meteor tracks. It is hard to say whether Figure 18 shows systematic gain and phase variations with bearing. The measurement errors in the relative phases and gains were <1° and <2% respectively on average, and <2° and 4% in all cases, so the scatter seen in Figure 18 is not due to statistical errors. We would need more meteor tracks to establish a continuous curve and to verify that the fluctuations in gain and phase really are due to a bearing dependence of the HF propagation properties. In addition, the measurement would be better performed with an array that could give some idea of the elevation angle.

In any case, the variations in Figure 18 show that the relative gains and phases vary by ±0.1 and ±5° respectively. Effectively, the relative gain and phase errors add to any complex amplitude A measured in an element, a 'noise' amplitude B with $|B| \sim 0.1|A|$.

Figure 18 may be compared to the NEC estimates of array coupling displayed in Figure 5. The only feature of Figure 18 that can be explained as array coupling is the decrease in relative gain of antenna 1 as the bearing angle α increases and the less pronounced increase in element-8 gain.

What could cause the variations shown in Figure 18? Nearby reflectors might cause some of these effects, but it would be surprising if the reflected signal had an amplitude ~10% of the direct wave. More likely, the explanation is that this is an effect of variations in ground conductivity. For ~300 m in front of the array, the ground was a level field with no obvious variations in soil condition, but there is no assurance that the soil depth was constant or that bedrock did not approach the surface.

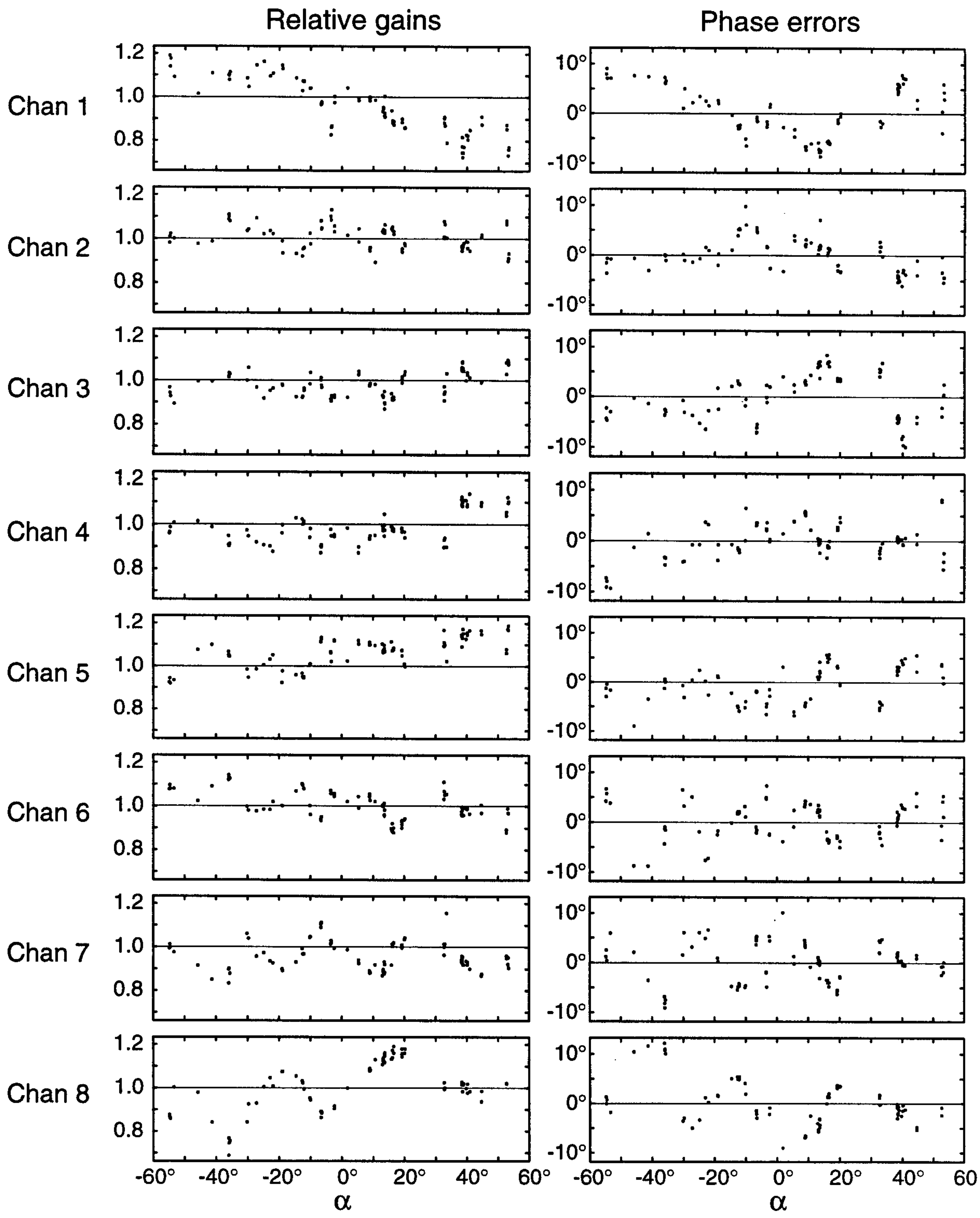

Figure 18. The bearing-dependent relative calibration deduced from meteor reflections. The relative gains are normalized so $\Sigma(gain_k)^2=8$ (except =7 for data where channel 8 was not working). The statistical uncertainty in the gains and phases are ~2% and ~1° respectively .

Table IV. The average phase offset in each channel determined from analysis of meteor tracks. This is the offset due to differences among the cables and antennas of the receive array. The phase offsets should be subtracted from the element phases after correcting for the receiver phase errors which are measured in loopback runs.

Channel	Average phase offset
1	-3.0°
2	0.7°
3	3.4°
4	0.9°
5	-2.9°
6	3.7°
7	-2.8°
8	-2.4°

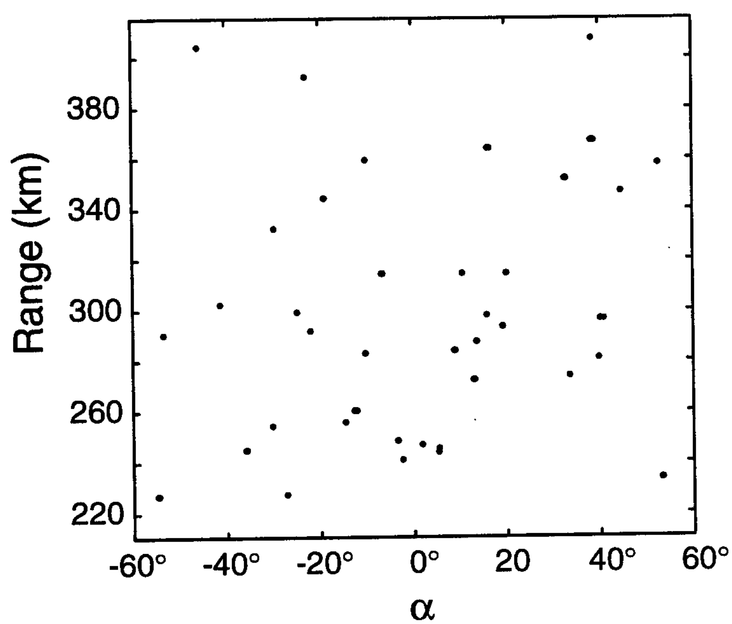

Figure 19. The ranges and bearings of the meteor tracks used in the relative calibration of the receive array. α is the angle left of boresight.

The Ottawa River was only ~600 m in front of the antennas. With an antenna height of 0.4λ, and a 10° elevation angle, the first Fresnel zone extends to ~140 m, while at 5° elevation it reaches 680 m. Thus the river may have had a small effect on the propagation for the lowest-angle reflections.

If this method is used to provide a bearing-dependent array calibration, more data should be used, and the array should be designed so the track elevation angle can be measured. This analysis used all of the data that showed significant numbers of meteor tracks, and was insufficient to provide unambiguous measurement of the phase and gain errors. By creating two lines of antennas at ~90° to each other, the elevation and azimuth angles could be determined, and it would become clear whether some of the variations seen in Figure 18 are due to signals arriving from different elevations.

Figure 18 and Table IV indicate that the errors are generally small, and that the major consequence of the miscalibration will be that power will spread away from the direction of a strong signal. This will make it harder to detect weak reflections that have the same range and Doppler shift as the strong signal, but a different bearing.

6. External noise and background signals

During the tests of the radar, three sources of background signals were observed : (i) external interference, (ii) meteors, and (iii) environmental clutter. While the meteor tracks were discussed extensively above in Section 5 as point-like sources for array calibration, we have not yet considered them as a source of background against which targets like aircraft and missiles must be detected.

6.1 External interference

At 24.5 MHz, the external interference is very different from the interference reported at lower frequencies in the HF band. In the autumn of 1998, when these measurements were made, the daytime ionosphere did not appear to support transmission near 25 MHz with the result that almost no distant sources of interference were observed. Since the ground wave is attenuated strongly over land at this frequency, the only source of interference was nearby transmitters and electrical equipment which operated only during the day.

The consequence was that we saw enhanced noise during the day and early evening, but there was essentially no interference at night. Figure 20 is a plot of the power observed with the transmitter off in one channel of the 8-element receive array at two times 8.5 hr apart. In both the noisy (late afternoon) and quiet (nighttime) data, the data were recorded as 256-point snapshots at a sampling rate of 10^5/s. The snapshot rate was 80/s. The power plotted in Figure 20 is the snapshot average (i.e. a 2560-μs average).

The noise data were analyzed in segments by applying gain and phase corrections to the 8 received signals, then calculating the 8×8 correlation matrix for each segment, and finally determining the eigenvalues and eigenvectors of the correlation matrices. The total signal power is the sum of the eigenvalues. If the noise is truly random and non-directional, the eigenvalues will all have roughly the same magnitude. On the other hand, highly directional, strong interference will lead to a correlation matrix with one eigenvalue much larger than the others, and in which the eigenvector represents the array response to a plane wave. (i.e. all elements of the vector have the same magnitude, and there is a constant phase difference between consecutive elements).

For the night-time data (quiet conditions), the correlation matrix indicated that the noise appeared random and non-directional. The largest eigenvalue was roughly 2.5 times the other eigenvalues, but it represented only 26% of the total power, and the eigenvector did not correspond to a received plane wave. This is expected since, as shown in Figure 15, the system electronics create ±20 kHz and ±40 kHz signals which would be coherent between channels.

During the lowest-noise segments of the daytime data, the largest eigenvalue had only 33% of the total power, and the eigenvector corresponded to a source 57° to the left of the boresight of the array. In the high-noise segments and in the spikes, the eigenvalue analysis showed that the largest eigenvalue had >95% of the total array power, and it corresponded to another source near the left end-fire of the array. Overall, the mean daytime noise shown in Figure 20 is only ~4 dB higher than the nighttime level, but it is so variable that the average does not mean much except where the output is

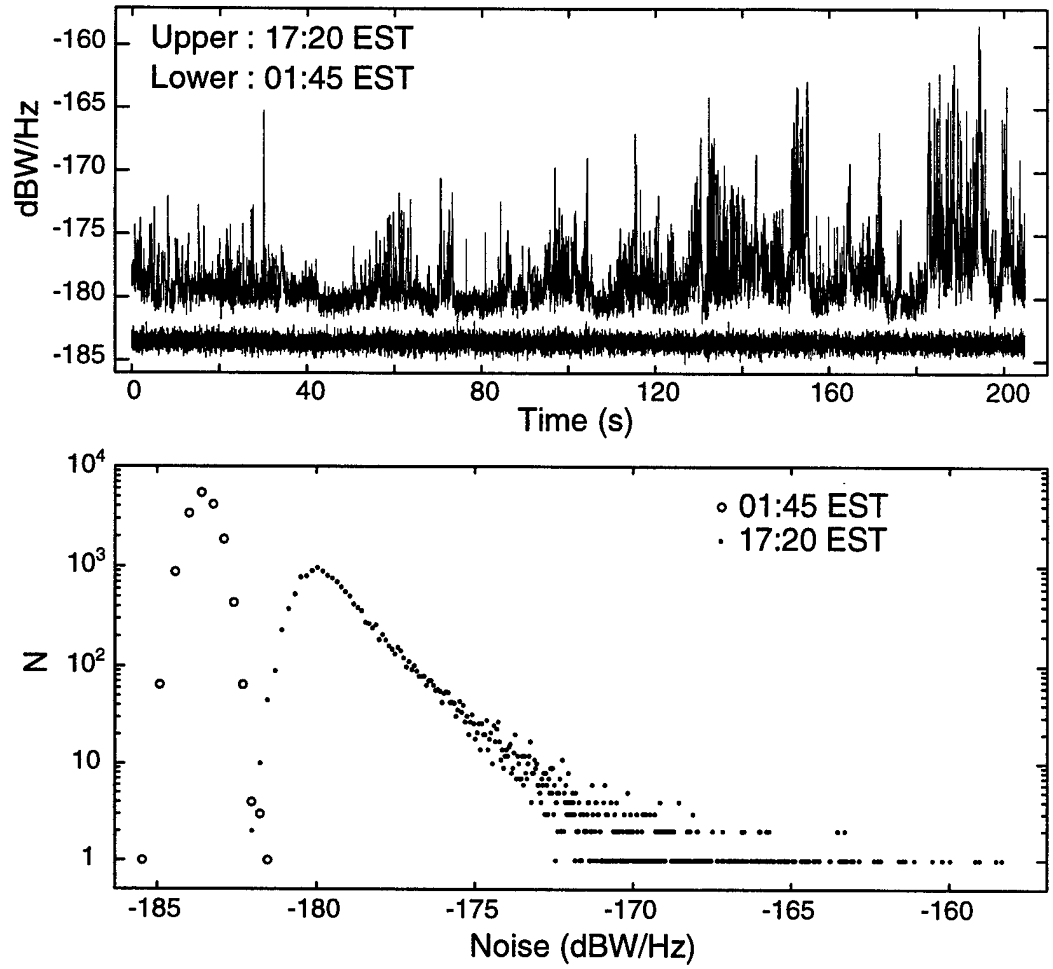

Figure 20. Noise data recorded on one antenna at 24.44 MHz on Nov.3/4 1998.
Top : 2560-μs averages of the noise power at two times of the day. The averages were calculated at a rate of 80/s.
Bottom : The same data plotted as a histogram. The bin width is 3.8×10^{-20} W/Hz. There are 16390 points in each histogram.

an average over many seconds of data. Doppler processing with a long coherent-integration time is an example of such averaging.

It is not possible to extrapolate the noise measurements reported here to other locations since the noise is due to the details of the local environment, and distant sources of interference have only a minimal impact on the radar performance, at least during periods near sunspot minimum where the ionosphere does not support propagation at 25 MHz. This day/night variation in the interference is in sharp contrast with the interference observed at lower frequencies where the improved ionospheric propagation at night results in a large increase in interference, while the daytime enhancement of the absorbing ionospheric D layer results in little day-time interference from distant sources.

6.2 Meteors

Meteors provide a background of point-like targets which may interfere with the detection of aircraft. The characteristics of meteor reflections were discussed in Section 5.4 above. Here we discuss briefly their contribution to the overall noise environment of the radar. Ref. [6] provides a more detailed discussion of the effect of meteors on HF radars.

Figure 21 is a plot of the Doppler power spectrum calculated from 6.4 s of the signal of one element of the receive array for the meteor track shown in Figure 17 above. The transmitted power was ~400 W with a peak antenna gain of ~6 dBi.(see Figure 3 above). The significant characteristic is that the power is confined to Doppler frequencies in the band $-10\ \text{Hz} < f_D < 10\ \text{Hz}$, and that the meteor track provides a huge signal within this band. Note that high-Doppler-shift reflections that might occur during formation of the meteor trail contribute almost nothing to the total signal power. This is not surprising since the segment of data shown in Figs. 17 and 21 was chosen because the reflection was strong, and strong reflections happen after the meteor trail is formed in situations where part of the trail is perpendicular to the line of sight to the radar.

To calculate the average effect of meteors, the spectral density must be multiplied by the probability that a track will appear in a particular segment of data. The rate at which strong meteor signals appear in the data is quite variable, but a reasonable guess is ~1/min on the 'forward' side of the receive array and between ranges of 100 and 400 km. Each track occupies one 1.5-km range bin, and appears with ~50% strength on the adjacent bins. With a 7-bit Barker code, a further 14% of the

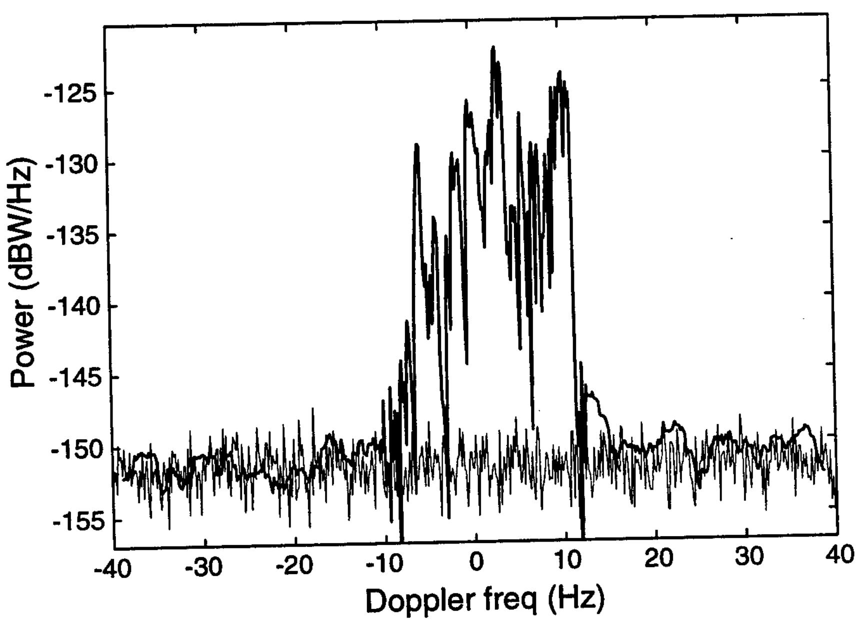

Figure 21. The Doppler power spectrum of the signal on one element of the receive array. The pulse rate was 80/s. The signal attenuation due to the matched filter has been taken into account in the calulation of received power.
Dark trace : Spectrum of 6.4 s of the meteor reflection shown in Figure 17. For f<-10 Hz and f>12.5 Hz, the spectrum has been smoothed with a 2.5-Hz window.
Light trace : Spectrum of the signal at the same time, but at ranges from 388 to 413 km.

signal energy appears in the range sidelobes. Then the probability that a particular 6.4-s segment of data will have a strong meteor track is low :

$$\text{Prob} \sim \frac{6.4\,\text{s}}{60\,\text{s}} \times \frac{(2.14\ \text{range bins}) \times 1.5\,\text{km}}{300\,\text{km}} = 0.0011 \quad .$$

Thus we conclude that the average power due to strong meteor reflections is ~30 dB lower than shown in Figure 21. However, echoes from overdense meteor tracks are transients that overwhelm other reflections, but that are only rarely present. The correct treatment may be to ignore the meteors most of the time, and to reject data where the meteor track obscures the target echo. However, in Doppler processing with long coherent integration times, it will not be possible to avoid meteors, and strong meteor tracks will appear as a rise in the environmental background for targets speeds ≤60 m/s.

The question of weak meteor tracks is important. They are probably much more frequent than the strong tracks. It is expected that the strong and the weak tracks have similar Doppler shifts ($-10\ \text{Hz} < f_D < 10\ \text{Hz}$), but that it might be difficult to single out the weaker tracks. If the weak tracks are present in significant numbers, then Doppler spectra of background noise should show a significant increase between -10 and +10 Hz. No such broad enhancement was seen in the data recorded with this radar in 1998.

6.3 Environmental clutter

At 24.5 MHz, strong reflections resulting in environmental clutter appeared occasionally at all ranges from 30 km to >600 km. We attribute them to reflections from stratospheric or mesospheric turbulence, possibly during atmospheric conditions that resulted in ducting, because the ionosphere cannot create reflections at ranges <100 km. As with radar investigations of meteor tracks, there is an extensive literature (e.g. Ref. [7]) on the application of HF and VHF radar to research on winds and turbulence in the atmosphere at altitudes ranging from a few km to ~100 km. Typically, the radars operate in the frequency range 40-50 MHz, and are directed upward with narrow transmit beams, in contrast with the portable radar described in this report which operates at 24.5 MHz, has a horizontally-directed radiation pattern (see Figure 3) and is not designed for atmospheric investigations.

In most of the data recorded in the autumn of 1998, environmental clutter was completely absent. The background data in Figure 21 are typical : no enhanced reflections appear near zero Doppler shift. On several runs, however, clutter was the dominant feature of the received signal. This section discusses the spectral and spatial character of the clutter.

Figure 22 shows the total received signal intensity for two runs recorded at 80 pulses/s. A delay of 1320 μs was added in the first run in order to check the system response at very long ranges. This was done under the mistaken assumption that only noise would be present in reflections with a 4-ms delay (600-km range). The power plotted in Figure 22 is the sum of power on all 8 receive-antenna elements averaged over 0.25-s (20-pulse) intervals :

$$P_{tot} = \sum_{k=1}^{8} \frac{I_k^2 + Q_k^2}{g_k^2} \quad .$$

g_k is the relative gain of channel k normalized to $\Sigma g_k^2=8$.

The dominant features of Figure 22 are three regions of enhanced reflections :

(i) near 440 km range and time=0-180 s,

(ii) a broad region covering all ranges up to 350 km at time 0, but reduced to ranges <140 km after 800 s

(iii) another broad region centred near 350 km at time 600 s, and moving to 270 km at 1100 s.

In addition to the enhanced areas, 'streaks' appear in Figure 22. These correspond to reflections where the source appears to stay in a fixed position.

Figure 23 shows the Doppler power spectra summed over antennas and averaged over the rectangular regions marked 1,..,4 in Figure 22. Data were recorded at a pulse rate of 80/s, but only the

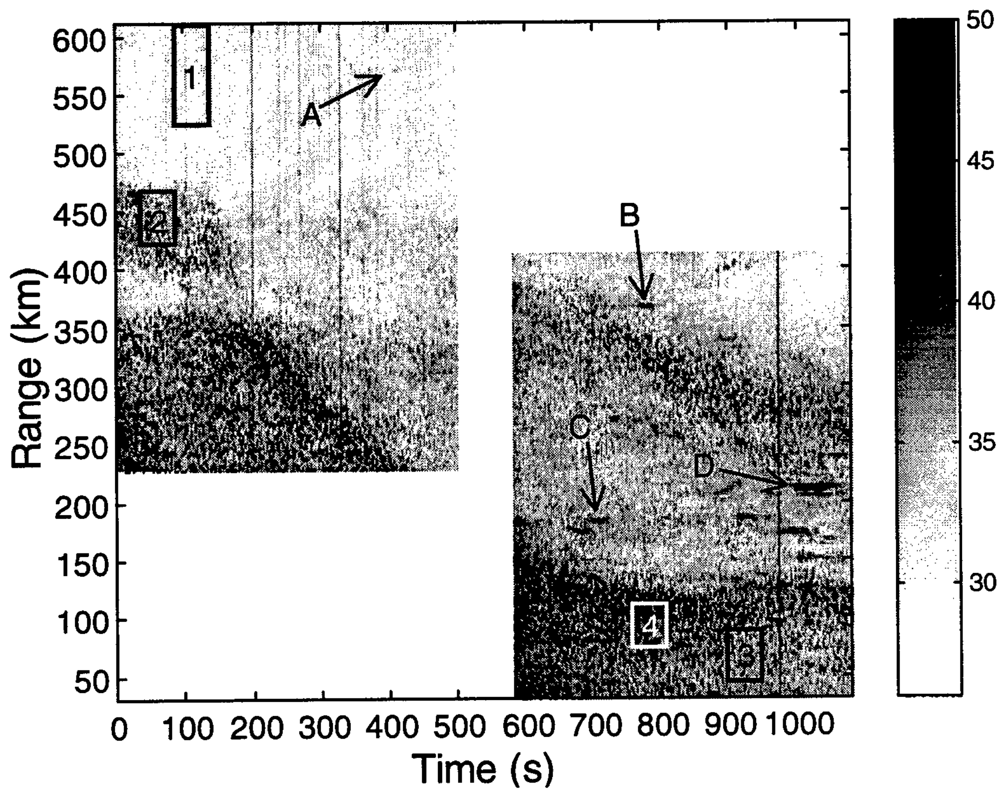

Figure 22. The total received power vs. time and range. A delay of 1320 μs was added to the first set of data. The signal power was summed over the 8 elements of the receive array and smoothed in 20-pulse averages (0.25 s). In low clutter conditions, the total received signal is 26.1 dB which corresponds to an average noise level of −182.4 dBW/Hz in each channel. The labeled areas and streaks are shown in more detail in Figures 22 and 23

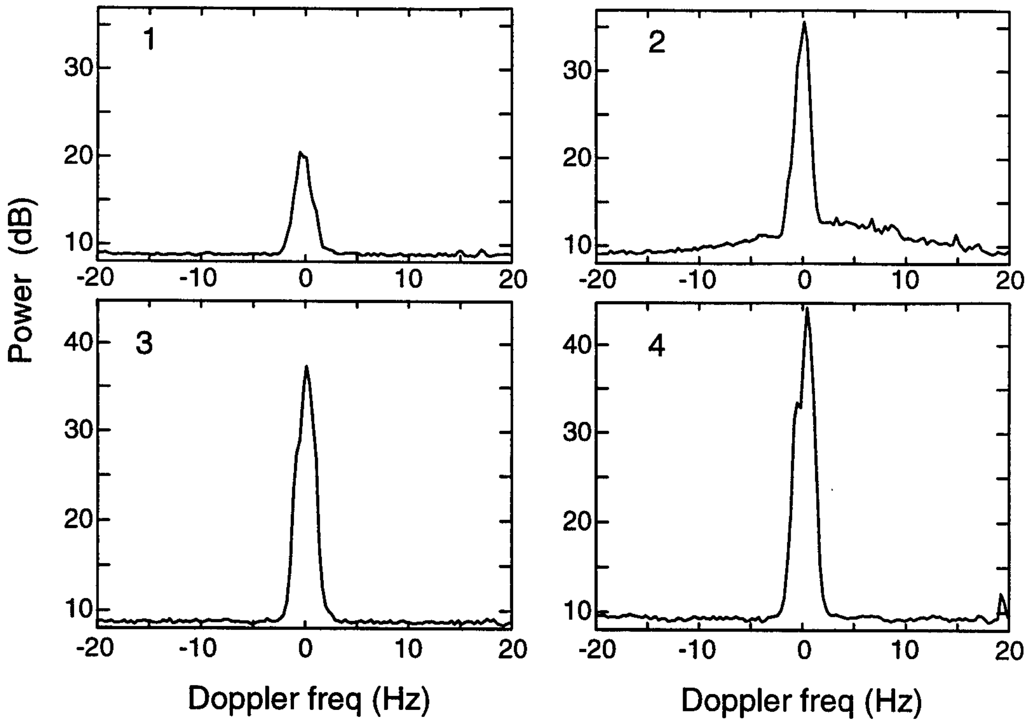

Figure 23. The Doppler spectra for the rectangular regions shown in Figure 22.

central half of the Doppler spectra is shown in the figure in order to make it easier to see features near f_D=0 Hz (the spectra for $|f_D|$>20 Hz were featureless). All spectra showed the same characteristics : the clutter power was concentrated in a broad peak between –2 and +2 Hz. Region 2 at 440 km also showed a second broad structure covering –10 to +15 Hz. For a 24.44 MHz radar, a 2-Hz Doppler shift amounts to a speed of only 12 m/s.

Figure 24 shows Doppler spectra calculated for the streaks marked A,B,C,D in Figure 22. In these cases, the spectra are dominated by a few narrow lines which stand above the broad peak seen everywhere in the data. Again, the targets are moving very slowly, with the narrow lines all having Doppler shifts <1 Hz (speeds <6 m/s).

Figure 25 shows three range/bearing plots of the echo intensities for two time segments of the data shown in Figure 22 and selected Doppler shifts. The data were analyzed in the standard way :

(1) The Fourier transform of the selected segment of data was calculated for each antenna and range bin,

(2) For each range bin and frequency element in the specified band of Doppler shifts, the bearing distribution of signal power was calculated from a Fourier transform over the 8 array elements. A simple trapezoidal taper was applied to reduce spectral leakage which would have resulted in enhanced bearing sidelobes.

Figures 24(a) and (c) show the distribution of the power in the main peak of the Doppler spectra. It is interesting to note that the dominant source of reflections maintained a bearing of ~20° to the right of the antenna boresight over a period of 900 s and ranges between 30 and 500 km. A second

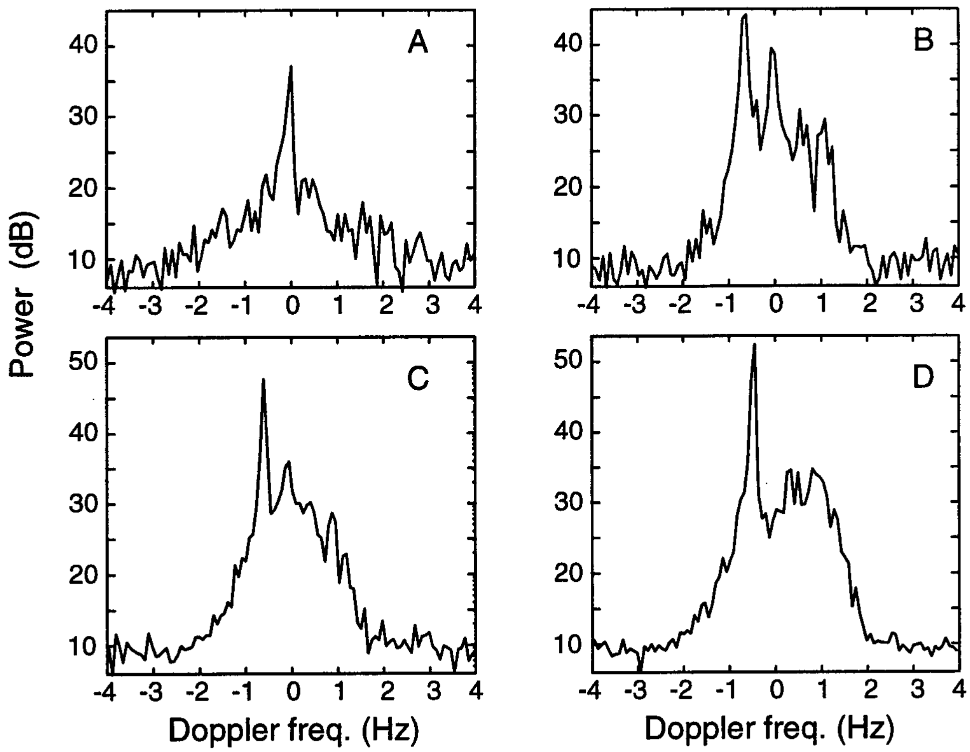

Figure 24. The Doppler power spectra of the streaks indicated by A,B,C,D in Figure 22. The power scale has the same normalization as in Figure 23.

'line' of sources also appears in Figure 25(c) at ~30° left of the antenna boresight. Figure 25(b) shows that the high-frequency part of the Doppler spectrum in Figure 23(2) is due dominantly to reflectors near 50° right of boresight at ranges of 400-500 km. In addition, a meteor track at 275 km and -12° appears in the high-Doppler shift plot, and a broad enhancement of the noise near the left endfire is visible. Section 6.1 discussed the external noise that appeared near the left endfire of the array.

For straight-line propagation, what is the altitude of the reflectors that create the environmental clutter displayed in Figures 22-25? Figures 3 and 26 (below) show that the antenna gain is cut off sharply when the elevation is <2°. If we assume that atmospheric refraction is approximated by taking the radius of the Earth to be 4/3 of its true value (i.e. take R_0=8490 km), then a reflector at >2° elevation and a range of 400 km must have an altitude of at least 23 km. At 600 km range, the altitude is at least 42 km. If the reflectors are in the main beam of the antenna (15° elevation), then the reflector altitudes are 112 and 175 km at ranges of 400 and 600 km respectively. These estimates of reflector altitude may be completely unrealistic however, since these data are probably evidence of ducting where the refraction of the 25-MHz radiation is considerably greater than predicted by the 4/3-radius rule.

We cannot rule out ionospheric reflection as the source of the clutter in spite of the fact that strong signals appeared at ranges as low as 30 km. All of the data that showed the clutter were

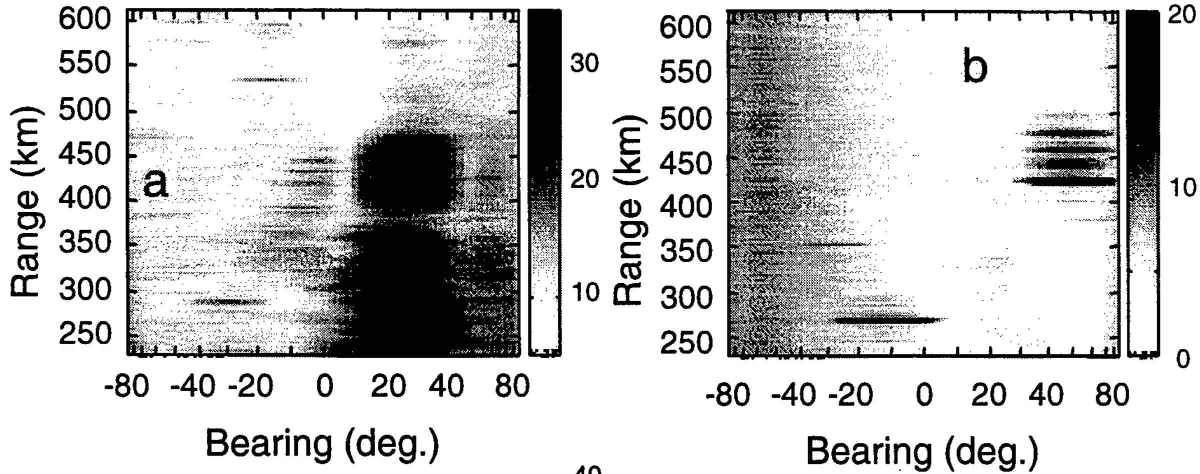

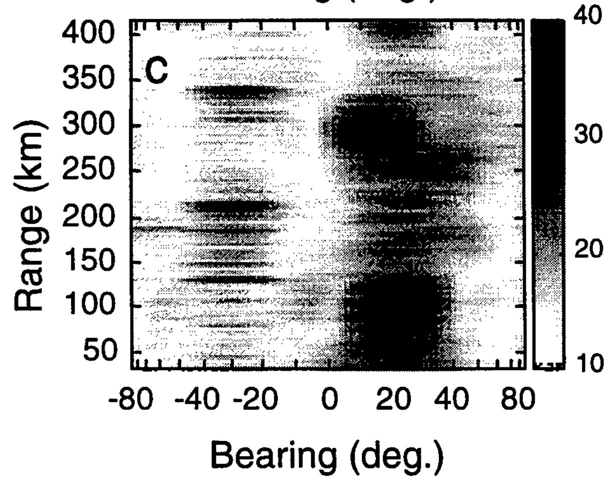

Figure 25. Range/bearing plots of some of the data shown in Figure 22-24 for selected times and Doppler shifts
(a) Time= 50-76 s, f_D*=-1.5 to +1.5 Hz.*
(b) Time= 50-76 s, f_D*=+3 to +10 Hz.*
(c) Time=890-916 s, f_D*=-1.5 to +1.5 Hz.*
The small bar beside the figures indicates the intensity in dB. The intensity scale is the same for (a),(b) and (c) but is not normalized to Watts.

recorded at 80 pulses/s, a rate chosen to match the data recorder (see Section 3.2.1 above), so reflectors at ranges of 1905 to 2487 km would also appear in the ranges displayed in Figures 22 and 25. This seems to be a very large range for a low-power system like the radar described here.

The clutter spectra displayed in Figures 22 and 23 show that the clutter will have little effect on detection of high-Doppler-shift targets ($|f_D|$>10 Hz), However, the environmental clutter may make it difficult to track targets that are moving tangentially to the line of sight.

7. Predicted performance

The portable radar described in this report was initially developed as a cheap, simple Line-of-Sight radar for detecting theatre ballistic missiles (TBMs). This section applies the radar equation to predict the performance of the existing system against a plausible target, and then discusses the performance that could be achieved with some improvements to the system.

7.1 Existing system

The radar equation for the signal-to-noise ratio for a single pulse is

$$\frac{S}{N} = \frac{G_t G_r \sigma \lambda^2}{(4\pi)^3 R^4} \frac{P_t}{P_n} \tag{12}$$

where G_t and G_r are the antenna gains, σ is the radar cross section, R is the distance to the target, P_t is the transmit-pulse power, and P_n is the received noise after pulse compression. The receive-array gain is included in G_r; receive array cable losses appear in P_n. We start by discussing the individual terms in the equation.

(i) P_t : Transmit Power : We have an 8-kW transmitter and a 1-dB loss between the transmitter and its antenna. The broadcast pulse is an 13-bit Barker code with 30-µs bits, smoothed with a 19-µs hanning function to ensure that almost all of the signal power lies within the ±50-kHz bandpass of the receiver electronics. Thus the transmitted power is

$$P_t = P_{\max} \times (\text{pulse - shaping loss}) \times (\text{cable loss}) = 5.4\,\text{kW} = 37.3\,\text{dBW} \quad .$$

With this pulse length, the radar would be operated at a pulse rate of 250/s giving a transmitter duty cycle of 10%.

(ii) P_n : Noise power. Section 5 and Table I listed noise levels referred to the receiver inputs; the quietest channel shows total noise of −183.6 dBW/Hz, while the average power is -182.6 dBW/Hz. We use the average noise in estimates of the array performance. The effective noise bandwidth after pulse compression is B=1/(13×30 µs)=2.56 kHz. In addition, there is a loss of ~3.5 dB (L_R=0.45) in the cables connecting the antennas to the receiver inputs. This gives the noise power referred to the antenna :

$$P_n = P_0 B / L_R = 3.1 \times 10^{-15}\ \text{W} = -145.0\ \text{dBW} \quad .$$

(iii) G_t, G_r : Antenna Gains. Figure 3 shows small-scale plots of the antenna gains at 24.1, 24.5 and 24.9 MHz and Figure 26 is a more detailed plot of the 24.5-MHz antenna gain as a function of elevation angle in the forward direction. The element gain falls by ~2.8 dB at ±60° azimuth.

G_r, the gain of the 8-element receive array, is 9.0 dB (= 10 log 8) higher than the transmit gain G_t.

(iv) σ : Target cross section. The target cross section is unknown, but reasonable estimates can be made if we model a small ballistic-missile target as a vertical conducting cylinder. For cylindrical targets of length 0.4-1.3λ, with the incident E-field parallel to the cylinder axis, the cross section lies in the range (0.2-0.8)λ^2. For the radar described here, λ=12.2 m, so targets of length 5-16 m, will have cross sections in the range 30-120 m^2 (14.8-20.8 dBm^2). This range of target lengths covers sounding rockets like the Black Brant, and TBM's such as the SCUD.

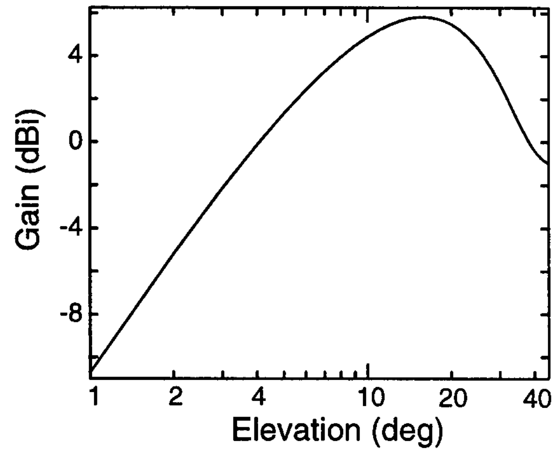

Figure 26. NEC calculation of the antenna gain in the forward direction at f=24.5 MHz. These data were plotted in a small-scale polar plot in Figure 3. θ is the elevation angle above the horizon.

More detailed and accurate estimates of the cross section can be made, but for the purposes of rough calculations, the estimate of σ~15-21 dBm^2 (σ~-7 - -1 dBλ^2) is adequate, ands we use σ=15 dBm^2 (i.e. the lower limit) for estimating the radar performance. Note however, that this estimate ignores the reduction in cross section as the ascending target tilts from vertical to horizontal. Note also that this estimate ignores reflections from the rocket exhaust plume.

Substituting these estimates of the transmit and noise powers, antenna gains and cross section into the radar equation allows calculation of the signal-to-noise ratio (SNR) for a single pulse. For the low-cross section case (σ=15 dBm^2=-7dBλ^2), Figure 27 shows the number of pulses that must be integrated coherently in order to achieve SNR=15 dB which we take as a reasonable detection threshold. Note that this SNR is based on the 'quiet' data displayed in Figure 20; P_n would be increased by 4 dB and the SNR reduced to 11 dB if the 'noisy' data were used to estimate the noise background.

For elevation angles of 10° and a target in the forward direction, Figure 27(a) shows that an SNR of 15 dB should be achieved after a 1000-pulse integration at 310 km range for a target on the boresight. Taking into account the 2.8-dB gain reduction at 60° off boresight, a 1000-pulse integration will detect the target at 225 km. Figure 27(b) shows that a 1000-pulse integration should detect targets between 4.7° and 35° elevation angles at 200 km, with <200 pulses required for targets between 9° and 24°. If the radar is operated at 250 pulses/s, this means that coherent integration times of ≤4 s will detect the ascending missile on boresight to ranges of 300 km and at ±60° to ranges of 225 km.

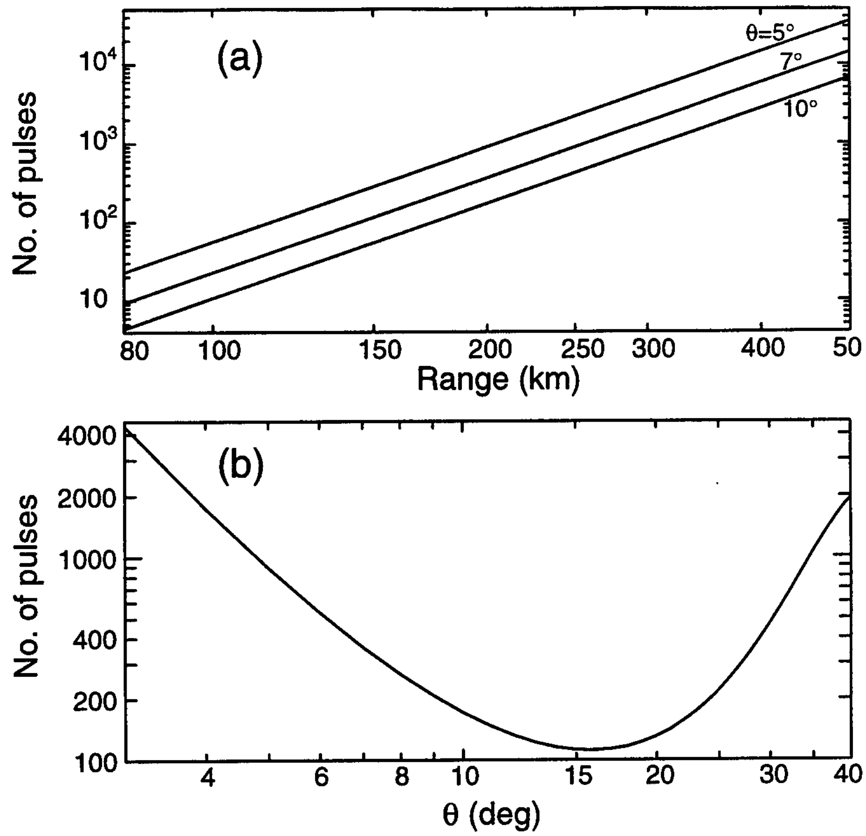

Figure 27. The number of pulses required to get an SNR of 15 dB for the radar and cross section parameters listed here. θ is the elevation angle above the horizon, and the target is on the array boresight. (a) Target elevation angles θ=5°, 7°, and 10°. (b) Target range = 200 km.

The uncertainty in the bearing estimate is derived from Ref. [8] :

$$\delta_{\alpha,n} = \frac{\sqrt{3}}{2\pi} \frac{\lambda}{L\sqrt{SNR \times \cos\alpha}}$$

where L is the length of the receive array and α is the azimuth angle. In the tests performed on the portable radar used an 8-element receive array with spacing d=6 m, giving L=7d=42 m. For a target at boresight (α=0°) and SNR=15 dB, this gives an angle uncertainty due to system noise $\delta_{\alpha,n}$=0.8°. The uncertainty due to system noise is much less than the array half-power beamwidth (Ref. [9]) :

$$\delta_{\alpha,B} = \frac{0.886\lambda}{N_{el}d} = 13° \quad .$$

It has been proposed to test this portable HF radar at White Sands Missile Range against Black Brant sounding rockets. It is expected that the radar will be erected at a range of ~160 km from the launch point and ~80 km from the impact point, with the antennas oriented to put the launch point at boresight. Figure 27 shows that we should detect the ascending target with a 300-pulse integration at 5° elevation and a 60-pulse integration at 10°.

7.2 System improvements : searching for dB's

Figure 27 shows that, for the portable radar parameters used in the previous section, the effective limit for the detection range of the system is ~300 km at 10° elevation angle(we assume a limit of 1000-pulses in the coherent integration). To improve the range to 600 km at 6° elevation, Figure 27 shows that we need to find 18 dB. There are several system improvements that could be made to improve the performance of the portable radar. They range from simply making the system bigger to major changes in the pulse compression and waveform coding.

(a) More receive antennas

The number of antenna could be increased from 8 to 16. This increase the signal-to-noise ratio for a given number of pulses by 3 dB, but would double the effort required to erect the system. Detection ranges would increase by a factor 1.19, or integration times would be reduced by a factor of 2.

(b) Reduce receiver noise.

The existing receive antennas are connected to the electronics by 100-m RG213 cables which attenuate signals by 3.5 dB. As a consequence, the system noise is dominated by the receiver noise during quite times of the day. By replacing the cables by Heliax LDF4 cables like the ones in use on the transmit antenna, the cable losses would be reduced to 1.1 dB from 3.5 dB.

The receiver/ADC noise with a 50-Ω terminator on the receiver input ranges from -185.6 to -184.0 dBW/Hz. The basic thermal noise at T=20C in the resistor is –203.9 dBW/Hz, so the receiver noise figure ranges from 18.3 to 19.9 dB. This can probably be reduced to 15 dB.

Adding preamps at the base of the antennas could boost the signals by ~8 dB, and ensure that the receive system is external-noise limited. This is probably the simplest and cheapest way to make the system external-noise limited.

We expect that the total noise referred to the antennas can be reduced by 4 dB from the levels observed during these tests.

(c) Higher transmitter peak power

In the existing portable radar, all of the transmit, receive and data-acquisition electronics are mounted in a single small trailer. If significantly-higher transmitter power is required than the present maximum of ~800 W, the transmitter amplifiers could not be mounted in the same trailer as the receivers, and the transmit antenna would have to be placed farther from the trailer than the current 90 m.

If the additional system complexity is acceptable in the portable system, a peak transmitter power level of ~20 kW could be achieved. By placing the transmitter amplifiers closer to the transmit anten-

na, transmitter cable losses could be eliminated. Thus we conclude that the pulse power could be increased from 5.4 kW as estimated above to ~17 kW, a 5.0 dB increase.

(d) Higher transmitter duty cycle and different pulse coding.

The existing system uses pulse compression of simple binary-phase-coded (BPC) pulses to achieve acceptable range resolution. With BPC pulses, the echo of the entire pulse must be compressed in order to make a simple interpretation of a reflection, so the target distance must be greater than c/2 times the length of the transmitted pulse. In the sample calculation above, the total pulse length after smoothing and filtering is ~420 μs. In addition, it takes a short time to turn off the transmitters so that the receivers can be turned on. The result is that the receivers are not turned on until ~440 μs after the start of the pulse and the radar has an eclipsing zone of ~66 km.

For binary-phase pulse coding the duty cycle and the minimum and maximum detection ranges and are related by

$$\text{duty cycle} \sim \frac{\text{min. range}}{\text{max. range}} = (\text{pulse rate}) \times (\text{pulse length})$$

Thus if a broad range of target distances is required the duty cycle must necessarily be low. The constraints on duty cycle imposed by the minimum and maximum ranges may result in less power being transmitted than the maximum transmitter rating.

A further consequence of the BPC pulse modulation is that the bandwidth of the transmitter and receiver electronics must be large enough to preserve the binary coding of the pulse. The portable radar has a bandwidth of ±50 kHz, although the effective noise bandwidth after pulse compression is much lower (2.6 kHz in the example of Section 7.1). The consequence is that the system is vulnerable to interference throughout a 100-kHz band. With a narrower electronic bandwidth, it might be possible to avoid some of the interference.

FM systems (Stepped FM, Continuous-wave FM or Interrupted-CW FM) offer improvements on the BPC pulses in situations where the broad bandwidth results in too much interference, or the restrictions on minimum and maximum ranges results in the transmitter operating at less than its maximum duty cycle. For an FM system, the basic restriction on pulse length and pulse rate is that the receiver should be enabled to receive all of the reflected energy from the most distant target of interest. That is, if the pulse length is τ and the maximum range is R, then the minimum pulse period T is

$$T = 1/\text{pulse rate} = \frac{2R}{c} + \tau \quad .$$

The minimum range is determined by the delay between the end of the transmit pulse and enabling the receivers. As an example, for a maximum range of R=500 km, a pulse rate of 180/s with a pulse length of 2200 μs will give a duty cycle of 40% and a pulse bandwidth of B=0.5 kHz + FM sweep. If

the power supply can operate at 40% duty cycle, this alone represents a factor 4 (6 dB) increase in the signal-to-noise ratio over the existing transmitter which is limited to 10%.

(e) Summary of improvements

The following improvements in SNR could be achieved :

More receive antennas	3 dB
Reduced receiver noise	4 dB
Increased transmitter power	5 dB
Increased duty cycle	6 dB
Total improvement	18 dB

7 dB of cheap improvements can be achieved by reduced receiver noise and more antennas. Increasing the signal-to-noise ratio by 7 dB would increase the detection range for a 1000-pulse integration by a factor 1.5, or reduce the integration time by a factor 5. Comparing to the results indicated in Figure 27, the 7-dB in effective noise reduction would increase the 1000-pulse, SNR=15 dB detection range from 210 km to 315 km at elevation $\theta=5°$, and from 255 km to 380 km at $\theta=7°$.

Increased transmitter power will require major revisions to the existing radar including large transmitter amplifiers and their power supplies located ~200 m from the receive-electronics trailer. Increasing the transmitter power will not require changes to the operation of the radar software.

Since the existing transmitters are limited to a duty cycle of ~10%, increasing the duty cycle will also require new transmitter amplifiers. Nevertheless, the option of converting to high-duty-cycle FM waveforms is an attractive way to gain a further 6 dB in the signal-to-noise ratio.

8. Summary and Conclusions

The 24.5-MHz Yagi antennas designed for use with the portable radar performed well and matched the NEC calculations of their performance.

The system performed well in tests in 1998. The electronics problems listed in Section 3.5 are not significant limitations on the system performance, except to the degree that they may indicate more serious problems in the electronics.

Absolute receiver noise was measured and radar runs with low average power allowed us to collect enough meteor data to provide a relative calibration of the receive array. Section 6.3 discussed an interesting environmental clutter originating in mesospheric or stratospheric turbulence, or possibly in ionospheric reflections.

Section 7.1 made estimates the performance of the existing system against small targets. The portable HF radar described in this report is ready for testing against TBM targets at medium ranges (~150 km).

Section 7.2 listed possible improvements to the system, two of which would require no changes to the radar electronics or controlling software :

(i) The system noise could be reduced by adding preamplifiers between the antennas and the receivers to make the system external-noise limited.

(ii) The number of elements in the receive array could be increased.

Other improvements in the performance against TBM's will require more transmit power, and changes to the radar electronics and pulse compression schemes.

Acknowledgements

The author is new to the field of HF radar, and has profited greatly from conversations with DREO staff members Hing Chan, Eric Hung, Ron Martin and William Read. Tony Ponsford, Rick McKerracher and Randy Howell of Raytheon Canada provided guidance and suggestions in the operation of the radar. Thaya Thayaparan provided a valuable introduction to the study of meteors and atmospheric physics using HF and VHF radar.

References :

1. G.J. Burke, "Numerical Electromagnetics Code (NEC) – Method of Moments;
   Part I: Program Description - Theory, Part II: Program Description – Code,
   Part III: User's Guide,
   Lawrence Livermore National Laboratory, Report UCID-18834, Jan.1981

2. Waters, W.M. and Jarrett,B.R., "Bandpass Signal Sampling and Coherent Detection", *IEEE Trans. Aerospace Electr. Sys.*, AES-18 (Nov.1982) pp.731-736
   Rice, D.W. and Wu,K.H., "Quadrature Sampling with High Dynamic Range", *IEEE Trans. Aerospace Electr. Sys.*, AES-18 (Nov.1982) pp.736-739
   Rader, C.M., "A Simple Method for Sampling In-Phase and Quadrature Components", *IEEE Trans. Aerospace Electr. Sys.*, AES-20 (Nov. 1984) pp.821-824

3. Farnett, E.C. *et al.*, "Pulse Compression Radar" Chapter 20, *Radar Handbook* (1970), M. Skolnik (ed.)

4. Oppenheim, A.V. and Schafer, R.W., *Digital Signal Processing*, pp.239-250 Prentice-Hall 1975
   The MathWorks, *MATLAB Signal Processing Toolbox User's Guide Version 4,* pp.2-18 1998

5. Oppenheim, A.V. and Schafer, R.W., *Digital Signal Processing*, pp.26-30 Prentice-Hall 1975

6. Jones, J. *et al.*, "An improved interferometer design for use with meteor radars", *Radio Science*, v.33, pp.55-65 , Jan. 1998, and references therein.
   Thayaparan, T., "Response of HF Radar to Meteor Backscatter", DREO Report (in review) August 1999.

7. Hocking, W.K., "System design, signal-processing procedures, and preliminary results for the Canadian (London, Ontario) VHF atmospheric radar", *Radio Science* v.32,pp. 687-706 March 1997.
   Carter, D.A. and Balsley, B.B., "The Summer Wind Field between 80 and 93 km Observed by the MST Radar at Poker Flat, Alaska (65°N)", *Journal Atmos. Sci.* v.39, pp.2905-2915 Dec. 1982

8. Swerling, P., "Radar Measurement Accuracy" Chapter 4, *Radar Handbook* (1970), M. Skolnik (ed.) See eq.(41)

9. Cheston, T.C. and Frank, J., "Array Antennas" Chapter 11, *Radar Handbook* (1970), M. Skolnik (ed.) See eq.(5)

UNCLASSIFIED

SECURITY CLASSIFICATION OF FORM
(highest classification of Title, Abstract, Keywords)

DOCUMENT CONTROL DATA

(Security classification of title, body of abstract and indexing annotation must be entered when the overall document is classified)

1. ORIGINATOR (the name and address of the organization preparing the document. Organizations for whom the document was prepared, e.g. Establishment sponsoring a contractor's report, or tasking agency, are entered in section 8.) Defence Research Establishment Ottawa	2. SECURITY CLASSIFICATION (overall security classification of the document, including special warning terms if applicable) UNCLASSIFIED

3. TITLE (the complete document title as indicated on the title page. Its classification should be indicated by the appropriate abbreviation (S,C or U) in parentheses after the title.)

Development of a Portable High-Frequency Radar (U)

4. AUTHORS (Last name, first name, middle initial)

Wilson, Harold S.

5. DATE OF PUBLICATION (month and year of publication of document) October 1999	6a. NO. OF PAGES (total containing information. Include Annexes, Appendices, etc.) 57	6b. NO. OF REFS (total cited in document) 9

7. DESCRIPTIVE NOTES (the category of the document, e.g. technical report, technical note or memorandum. If appropriate, enter the type of report, e.g. interim, progress, summary, annual or final. Give the inclusive dates when a specific reporting period is covered.)

Technical Report

8. SPONSORING ACTIVITY (the name of the department project office or laboratory sponsoring the research and development. Include the address.)

Defence Research Establishment Ottawa, 3701 Carling Ave., Ottawa, Ont. K1A 0Z4

9a. PROJECT OR GRANT NO. (if appropriate, the applicable research and development project or grant number under which the document was written. Please specify whether project or grant) 05AB11	9b. CONTRACT NO. (if appropriate, the applicable number under which the document was written)
10a. ORIGINATOR'S DOCUMENT NUMBER (the official document number by which the document is identified by the originating activity. This number must be unique to this document.) DREO TR 1999-108	10b. OTHER DOCUMENT NOS. (Any other numbers which may be assigned this document either by the originator or by the sponsor)

11. DOCUMENT AVAILABILITY (any limitations on further dissemination of the document, other than those imposed by security classification)

(x) Unlimited distribution
( ) Distribution limited to defence departments and defence contractors; further distribution only as approved
( ) Distribution limited to defence departments and Canadian defence contractors; further distribution only as approved
( ) Distribution limited to government departments and agencies; further distribution only as approved
( ) Distribution limited to defence departments; further distribution only as approved
( ) Other (please specify):

12. DOCUMENT ANNOUNCEMENT (any limitation to the bibliographic announcement of this document. This will normally correspond to the Document Availability (11). However, where further distribution (beyond the audience specified in 11) is possible, a wider announcement audience may be selected.)

Unlimited

13. ABSTRACT (a brief and factual summary of the document. It may also appear elsewhere in the body of the document itself. It is highly desirable that the abstract of classified documents be unclassified. Each paragraph of the abstract shall begin with an indication of the security classification of the information in the paragraph (unless the document itself is unclassified) represented as (S), (C), or (U). It is not necessary to include here abstracts in both official languages unless the text is bilingual).

The Surface Radar Section of DREO is developing a portable HF radar. The report presents an overview of the radar and analysis of a series of tests done in 1998. The equipment including antennas and electronics is described. A series of electronics problems was encountered, but none of them have a significant effect on the operation of the system. The receiver system was calibrated using loopback runs, source measurements and meteor reflections. Measurements of interference, meteors and environmental clutter at 24.5 MHz are presented. The results of the tests are used to estimate the performance of the portable radar in Line-of-Sight mode against theatre ballistic missiles.

14. KEYWORDS, DESCRIPTORS or IDENTIFIERS (technically meaningful terms or short phrases that characterize a document and could be helpful in cataloguing the document. They should be selected so that no security classification is required. Identifiers such as equipment model designation, trade name, military project code name, geographic location may also be included. If possible keywords should be selected from a published thesaurus. e.g. Thesaurus of Engineering and Scientific Terms (TEST) and that thesaurus-identified. If it is not possible to select indexing terms which are Unclassified, the classification of each should be indicated as with the title.)

High-Frequency radar
HF
Radar electronics
High-Frequency noise
Atmospheric interference
Meteor radar reflections